Article:
Zirks, E, Krom, M orcid.org/0000-0003-3386-9215, Schmiedl, G et al. (5 more authors) (2021) Redox evolution and the development of oxygen minimum zones in the Eastern Mediterranean Levantine basin during the early Holocene. Geochimica et Cosmochimica Acta, 297. pp. 82-100. ISSN 0016-7037

https://doi.org/10.1016/j.gca.2021.01.009

Redox evolution and the development of oxygen minimum zones in the Eastern Mediterranean Levantine basin during the early Holocene

Authors: Eleen Zirks[1,2], Michael Krom [3,4], Gerhard Schmiedl[5], Timor Katz[6], Yijun Xiong[4], Lewis J. Alcott[7], Simon W. Poulton[4], Beverly Goodman-Tchernov[1]

1. Department of Marine Geosciences, Leon H. Charney School of Marine Science, University of Haifa, Haifa 3498838, Israel

2. MARUM, Center for Marine Environmental Sciences, University of Bremen, Germany

3. Morris Kahn Marine Research Station, Department of Marine Biology, Leon H. Charney School of Marine Science, University of Haifa, Haifa 3498838, Israel

4. School of Earth and Environment, University of Leeds, Leeds, LS2 9JT, UK

5. Center for Earth System Research and Sustainability, Institute for Geology, University of Hamburg, Hamburg 20146, Germany

6. National Institute of Oceanography, Israel Oceanographic Limnological Research, POB 1080, Haifa, Israel

7. Department of Geology and Geophysics, Yale University, New Haven, USA

email addresses

Eleen Zirks eleen.zirks@gmail.com

Michael Krom M.D.Krom@leeds.ac.uk

Gerhard Schmiedl gerhard.schmiedl@uni-hamburg.de

Timor Katz Timor@ocean.org.il

Yijun Xiong eeyx@leeds.ac.uk

Lewis Alcott lewis.alcott@yale.edu

Simon Poulton S.Poulton@leeds.ac.uk

Beverly Goodman-Tchernov bgoodman@univ.haifa.ac.il

Corresponding Author is Michael Krom

Abstract

Oxygen Minimum Zones (OMZs) are expanding in modern oceans due to anthropogenically-driven climate and environmental change. In the Eastern Mediterranean Sea (EMS), OMZs developed in the early Holocene as a result of decreased intermediate water ventilation, increasing temperature, and increased Nile discharge and primary productivity. Here, we report benthic foraminiferal numbers (BFN) and species abundances, together with redox-sensitive trace metals (RSTM), and iron and phosphorus speciation from two sediment cores sampled at intermediate depths (1200 and 1430 m) from the SE Levantine shelf. The main aim of our study is to better understand the sequence of redox changes during sapropel S1 deposition caused by biogeochemical processes affecting the sapropel intermediate water mass. The use of benthic foraminifera indices (diversity and oxygen) together with iron speciation and RSTM (V, Mo and U) enables detailed description of the changing oxygen/redox status of the overlying water. Prior to sapropel S1 deposition at ~10.2 ka BP, RSTM suggest that the overlying water was well oxygenated, but benthic foraminifera numbers (BFN) suggest that oxygen levels had already begun to decrease. There was then a pulse of increased export carbon from the enlarged Nile flood plume, as shown by increased BFN at the beginning of sapropel S1. Shortly after, RSTM and Fe-S systematics suggest that the water column transitioned from dysoxic to anoxic, non-sulfidic. Anoxic conditions then persisted at 1200 m depth, but RSTM and benthic foraminifera indices suggest that deeper waters at 1430 m were more likely dysoxic, until the 8.2 ka BP global cooling event. The benthic foraminifera and inorganic redox proxies then suggest a second period of anoxic, non-sulfidic conditions, with a gradual return to well ventilated waters at the end of sapropel deposition at ~6 ka BP. There was enhanced burial of authigenic P throughout sapropel deposition, derived from the deposition and subsequent release of organic-P and iron bound-P during diagenesis. Phosphorus recycling from the sediment and in the overlying water column added reactive P to these mid-depth waters, a process which has the potential to result in a positive feedback in systems where such waters are upwelled into the photic zone. The past EMS thus represents a template which can be used to predict biogeochemical changes in settings that evolve towards anoxic, non sulfidic conditions, which may occur in some areas as modern climate and environment change causes the continued expansion of modern OMZs and hypoxic areas adjacent to modern major rivers.

Keywords: Sapropel, P cycling, Redox evolution, Benthic foraminifera, Eastern Mediterranean

1. INTRODUCTION

One strategy to predict the potential effects of anthropogenic activities on the environment and climate is to study geologically recent episodes of natural climate change and ensuing biogeochemical changes. One of the most dramatic locations to study such effects is the Eastern Mediterranean Sea (EMS), where during the late Holocene, the ultraoligotrophic water column changed to deeper water anoxia and back again over a period of ~5000 years, resulting in the deposition of organic-rich sapropelic sediments (De Lange et al., 2008).

At present, the circulation in the EMS is anti-estuarine (Pinardi and Masetti, 2000). Atlantic surface water flows into the EMS through the Straits of Sicily and then flows eastward. Due to strong net evaporation, the Atlantic surface water becomes progressively more saline as it flows to the east. In winter, the surface water cools and downwells to form Levantine intermediate water (LIW), which flows westwards, eventually exiting through the Straits of Sicily. Eastern Mediterranean deep water is formed in the Adriatic Sea in winter and has a residence time of ~120 years (Schlitzer et al., 1991). This water mass remains fully oxic throughout the basin, with levels of 60-80% O_2 saturation (Emeis et al., 1996).

In the relatively recent geological past (~10.8-6 kyr BP), however, the oxygen status of deep water in the EMS was very different (De Lange et al., 2008). As a result of insolation forcing, the climate in both N. Africa and the Mediterranean basin was more humid, and the physical circulation altered dramatically. The deep water below 1800 m became stagnant and euxinic (anoxic with free H_2S; De Lange et al., 2008), while the water structure above 500 m was similar to that of the modern EMS, albeit probably with a longer residence time (Myers et al., 1998; Stratford et al., 2000; Zirks et al., 2019). During this period, a distinct sapropel intermediate water (SIW) mass existed between 500 to 1800 m, which was formed in the Aegean and flowed into the southern Adriatic and the S.E. Levantine basin (Zirks et al., 2019).

Coincident with the formation of sapropel S1, the Inter Tropical Convergence Zone (ITCZ) moved north during the African Humid Period (DeMenocal et al., 2000), resulting in increased discharge from the river Nile (van Helmond et al., 2015; Mojtahid et al., 2015; Zwiep et al., 2018). Together with a regional increase in rainfall, this caused reduced surface water salinity in the EMS, reduced ventilation rates in the intermediate water, and stagnation in the deep water of the EMS. The maximum Nile flow, which was considerably higher compared to the modern Nile (Rossignol-Strick et al., 1982; Wu et al., 2019), resulted in a more extensive reduced salinity Nile plume off the Israeli coast (Hennekam et al., 2015). This increased Nile flow supplied abundant nutrients, resulting in higher primary productivity and thus enhanced export of labile organic carbon into intermediate levels (Zwiep et al., 2018). As the SIW flowed away from its Aegean source, decomposition of this labile carbon reduced the dissolved oxygen content, such that in the S.E. Levantine basin oxygen was largely (or entirely) consumed, resulting in

the development of two oxygen minimum zone (OMZ) intervals separated by a short period of partial reventilation (Zirks et al., 2019).

Several facets of the environmental response of the EMS during sapropel S1 formation are of relevance to the modern ocean. One of the consequences of modern climate change is an expansion of OMZs in the intermediate water of several parts of the ocean (Diaz and Rosenberg, 2008; Stramma et al., 2008; Breitburg et al., 2018). At present, OMZs have only reached the level of severe hypoxia with major denitrification (Breitburg et al., 2018; Levin, 2003), but the future response of OMZs to continued environmental perturbation remains unclear. In addition, another important consequence of modern anthropogenic change is an increased pollutant nutrient flux down many major rivers to the adjacent coastal zone (Ludwig et al., 2009). This is strikingly similar to the increased nutrient influx that occurred in the S.E. Levantine basin as a result of increased weathering in the Nile catchment during deposition of sapropel S1. In many locations these anthropogenic changes have resulted in areas of hypoxia on the adjacent coastal shelf, for example in the Gulf of Mexico adjacent to the Mississippi delta (Shi and Wang, 2009; Kolker et al., 2014), the East China Sea near the Yangtze river outflow (Li et al., 2002; Duan et al., 2008), and in the Bay of Bengal (Satpathy et al., 2013). At present, although these areas of hypoxia exist and are expanding, they have remained localised to the coastal shelf and have not expanded to intermediate depths. Therefore, detailed study of the response of marine settings adjacent to major river systems, such as the EMS during sapropel S1 formation, may provide important insight into the potential future behaviour of the modern ocean in a progressively warming and nutrient-rich world.

Here, we utilize biotic (benthic foraminifera) and inorganic geochemical proxies to determine the changing oxygen content of the water column during sapropel S1 formation. We focus on two cores sampled adjacent to the Israeli coast at depths of 1200 m and 1430 m, within the depth zone of SIW. We use Ba/Al and TOC to define the beginning and end of sapropel S1, and the AMS ^{14}C dating of planktonic foraminifera to determine sedimentation rates. Detailed study of the abundance and diversity of benthic foraminifera are used, in combination with Fe speciation and redox-sensitive trace metals (V, U and Mo), to determine the evolving redox state of the water column. Together with data collected from previous cores, these results are used to determine the spatial and temporal evolution of SIW across the coastal shelf under the Nile plume. We additionally report P speciation data to identify nutrient feedbacks and controls on the chemical evolution of water column redox conditions.

2. MATERIALS AND METHODS

2.1. Samples

Cores EZ17G5 (1200 m water depth, 32°18.19070'N, 34°15.20420'E) and ME0318 (1430 m water depth, 32°47.51667'N, 34°22.38333'E) were collected in the Eastern Mediterranean Levantine basin from the *R/V Mediterranean Explorer* in March 2017 and 2018, respectively (Figure 1). Core EZ17G5 was 224 cm long, and core ME0318 was 193 cm long. The cores were sampled the day after collection, split in half, and subsampled every centimetre into plastic containers, followed by freeze drying. The freeze-dried samples that were used for Fe and P speciation were stored in a freezer at -4°C until analysis, while the samples for major element and other analyses were stored at room temperature. The data from these two cores are compared with results from previously published cores (Figure 1), including PS009PC at 552 m water depth (Hennekam and de Lange, 2012; Hennekam et al., 2014), SL112 at 892 m water depth (Kuhnt et al., 2008; Schmiedl et al., 2010), 9505 at 884m water depth, and MD04-2722 at 1780 m water depth (Tachikawa et al., 2015).

2.2. Age model

Surface-dwelling planktic foraminifera samples from each core were analysed for their ^{14}C Accelerator Mass Spectrometry (AMS) age by Direct AMS, USA. Ages were calibrated using the marine mode of Calib 7.0.4 (Stuiver and Reimer, 1993). Linear regression was found to best fit the data and was therefore chosen to calculate ages (Figure 2). The data used to develop these linear regression plots is given in the Supplementary Information (Table S1). Since sample 94-95 from EZ17G5 has a corrected age of ~8.2 ka BP, which is a recognised time horizon related to a known global cooling event (Rohling and Pälike, 2005), we determined the age model for this core via two linear regressions, one from 0 to 95 cm, and the other from 95 cm until the end of the core.

2.3. Foraminifera analyses

Benthic foraminifera were separated from the >125 µm fraction at 1 cm resolution throughout the depths identified as sapropel, and at 1-2 cm resolution above and below the sapropel interval. Generally, the entire >125 µm fraction was used to achieve a sufficient number of benthic foraminifera for reliable faunal analyses. Foraminifera were identified at species level (see Figure S1-3), and the benthic foraminifera number per gram (BFN) was calculated. The Shannon-Weaver Diversity Index (H(S), Div) was calculated according to Buzas and Gibson (1969) based on the proportion of each species. Species with low occurences do not contribute greatly to the value of H(S), while species high in numbers contribute more. The highest Div value is given when all species have the same frequency (Buzas and Gibson, 1969). The oxygen index (OI) was calculated as the ratio between the relative abundance of high oxygen indication benthic foraminifera (e.g., *Miliolid* spp., *Gyroidinoides orbicularis*) and species indicating low oxygen (e.g., *Fursenkoina* spp., *Globobulimina* spp.), together with the normalized diversity (Schmiedl et al., 2003; Schmiedl et al., 2010).

2.4. Inorganic analyses

For the analysis of total organic carbon (TOC), about 45 mg of dry, ground sediment was pre-treated with 5% (vol/vol) HCl to remove inorganic carbon. After this treatment, samples were dried at 60°C and then combusted in an oxygen stream at 950°C. The samples were analysed with a Skalar Primacs^{SLC} Analyzer at the University of Haifa, Israel. Tests on a series of replicate samples (n = 6) gave a relative standard deviation (RSD) of ±8.3%. X-Ray fluorescence (XRF) was used to determine major and trace elements. Between 2.0-2.5 g of dried sediment was ground into fine powder and measured with an ED-XRF in a vacuum chamber. The precision and accuracy estimates for the major and minor elements are given in Table S2. For core EZ17G5, the resolution of XRF measurements was 1 cm within the sapropel zone, and 2 cm below and above, and for core ME0318 samples were measured every 2 cm.

The Fe speciation methods were developed from Poulton and Canfield (2005) and Canfield et al. (1986), as used by Zegeye et al. (2012), Goldberg et al. (2012) and Xiong et al. (2019). The procedure targets six operationally defined phases, with steps I-III performed sequentially (for extraction details see Table S3, which also reports target Fe phases and the precision of each extraction based on replicate extractions). The reduced iron extracted in step I was measured by spectrophotometer via the ferrozine method (Stookey, 1970), while the other unsulfidized Fe phases were measured by AAS. These extractions target unsulfidized reduced solid phase Fe (e.g., surface-bound Fe(II) and easily soluble reduced Fe minerals such as Fe(II) phosphates; $Fe(II)_{unsulf}$), highly reducible ferric oxides (e.g., ferrihydrite; Fe_{ox1}), crystalline Fe (oxyhydr)oxides (e.g., goethite and hematite; Fe_{ox2}) and mixed ferrous/ferric oxides (e.g., magnetite; Fe_{mag}). Sulfide bound as acid-volatile sulfur (Fe_{AVS}) and pyrite (Fe_{py}) was extracted by the two-step acid Cr(II) method and trapped as Ag_2S, followed by weighing of the precipitate and stoichiometric conversion to Fe concentrations (Canfield et al., 1986). The total concentration of Fe present as sulfide phases (Fe_{sul}) was then calculated as the sum of Fe_{AVS} and Fe_{py}.

The total pool of Fe that is considered highly reactive (Fe_{HR}) to biotic and abiotic reduction in near-surface environments (Canfield et al., 1992; Raiswell and Canfield, 1998; Poulton et al., 2004) was calculated as:

$$Fe_{HR} = Fe(II)_{unsulf} + Fe(III)_{ox1} + Fe(III)_{ox2} + Fe_{mag} + Fe_{sul} \quad (1)$$

The sequential extraction method (SEDEX) for different phosphorus phases was modified from Ruttenberg (1992). Five sedimentary P reservoirs were extracted by different reagents as detailed in Table S4. Iron-bound P (P_{Fe}) was determined via ICP-OES, due to interference of citrate with the spectrophotometric determination of phosphate. All other P phases were determined via the

194 molybdate blue method (Koroleff, 1976) on a Thermo Genesys 6 spectrophotometer at 880 nm
195 wavelength. Reactive P ($P_{reactive}$) was calculated as:

196 $$P_{reactive} = P_{sorb} + P_{Fe} + P_{aut} + P_{org} \quad (2)$$

197

198 **3. INTERPRETATIONAL REDOX FRAMEWORK**

199 Benthic foraminifera can be grouped into three main categories: epifaunal species which live on the
200 sediment surface, shallow infaunal species that live within the upper 2-3 cm of the sediment, and deep
201 infaunal species which live deeper in the sediments (down to ~9 cm). According to the TROX-model,
202 epifaunal species require high oxygen levels, while shallow and deep infaunal species require
203 progressively less oxygen (Jorissen et al., 1995; Jorissen, 1999). These distinctions can be used to
204 determine relative oxygen levels in the overlying water (Table 1). In addition, diversity and oxygen
205 indices were used to determine changes in the oxygen content. Generally, high Div and OI indicate
206 oxygenated conditions, whereas reduced Div indicates highly specialized fauna, and an OI of ~0.5
207 reflects reduced oxygen content. Finally, when Div and/or OI are zero, all benthic foraminifera have
208 died, suggesting anoxic conditions. However, deep infaunal species can migrate to shallower habitats,
209 and shallow infaunal species can migrate to epifaunal habitats, depending on oxygen and food supply
210 within the sediment and at the sediment-water-interface. In addition, Div (and hence OI) can also
211 change when the food supply drops, without concomittent changes in oxygen content (Schmiedl et al.,
212 2003).

213 To provide more detailed information on the precise redox state of the overlying water column, we
214 utilize iron speciation (Poulton and Canfield, 2005), which is commonly used to distinguish oxic,
215 ferruginous (anoxic, Fe-rich) and euxinic (anoxic, sulfidic) water column conditions. In this context,
216 Fe_{HR}/Fe_T ratios <0.22 provide robust evidence for deposition from an oxic water column, ratios >0.38
217 suggest anoxic water column conditions, and ratios from 0.22-0.38 are considered equivocal (Poulton
218 and Canfield, 2011; Poulton, 2021). For samples deposited under anoxic water column conditions,
219 Fe_{sul}/Fe_{HR} ratios can be used to distinguish euxinic from ferruginous conditions (Poulton and Canfield,
220 2011), whereby Fe_{sul}/Fe_{HR} <0.7 is commonly taken as the threshold for distinguishing ferruginous
221 settings, and Fe_{sul}/Fe_{HR} >0.8 denotes euxinia. However, based on several geochemical proxies,
222 Benkovitz et al. (2020) have recently suggested that for Eastern Mediterranean sapropel deposition,
223 Fe_{sul}/Fe_{HR} >0.6 (combined with Fe_{HR}/Fe_T >0.38) may be more appropriate for recognizing euxinic
224 depositional conditions, and this lower threshold is also supported by analyses of euxinic Baltic Sea
225 sediments (Hardisty et al., 2016; see Poulton, 2021).

We also use V, Mo and U (normalized to aluminium) to provide additional insights into water column redox conditions. Vanadium is commonly transported to sediments as the vanadate ion ($H_2V(VI)O_4^-$) adsorbed onto Mn oxides. Under dysoxic porewater conditions, where Mn oxides are reduced to Mn^{2+}, V is commonly released from sediments (Emerson and Huested, 1991; Nameroff et al., 2002). By contrast, under anoxic conditions, the vanadate released following Mn oxide reduction is reduced to the vanadyl ion ($V(IV)O^{2+}$), which is highly surface-reactive and tends to be retained in the sediment (Emerson and Huested, 1991). Molybdenum is transported to the ocean as the molybdate anion (MoO_4^{2-}) and is largely unreactive in oxic settings, with the main removal pathway to the sediments being through uptake by Fe-Mn (oxyhydr)oxide minerals (Bertine and Turekian, 1973). By contrast, if a critical threshold of free H_2S is met under anoxic conditions, the molybdate anion is converted to particle-reactive thiomolybdate (Helz et al., 1996; Wagner et al., 2017), leading to significant Mo enrichment in the sediments (Emerson and Huested, 1991; Helz et al., 1996; Erickson and Helz, 2000; Scholz et al., 2013). Unlike Mo, U is preferentially buried in sediments deposited beneath anoxic bottom waters regardless of whether euxinic or ferruginous conditions dominate, as U reduction primarily occurs in the sediments, not in the water column (Anderson et al., 1989; Klinkhammer and Palmer, 1991). Our combined geochemical approach thus offers the possibility of defining spatial and temporal variability in the precise redox chemistry of SIW as it evolved.

4. RESULTS

4.1. Major elements

The general trends for TOC and Ba/Al are similar between the two analysed sediment cores (Figure 3). TOC and Ba/Al start to increase from ~10.2 ka BP, with a small decline at ~8.2-7.6 kyr BP in core ME0318 and ~8.2-7.8 kyr BP in core EZ17G5, followed by a gradual decline to lower levels, with Ba/Al returning to pre-sapropel levels at ~6 ka BP.

V/Al ratios show similar, but subtly different, trends in the two cores (Figure 3), with values that are initially low (below average shale; Turekian and Wedepohl, 1961) before a large peak, which tails off more slowly in core ME0318 (V/Al ratios reach peaks of 35 at ~9.5 ka BP in EZ17G5, and 25 at ~9.7 ka BP in ME0318). In EZ17G5, there is subsequently a smaller peak in V/Al (~16) at ~8 ka BP. For both cores, U/Al ratios increase gradually, from values that are initially similar to average shale, before reaching a general maximum coincident with the point at which V/Al ratios return to background levels (~8.8 ka BP in ME0318, and ~9.3 ka BP in EZ17G5). These maxima in U/Al then persist before a gradual decline to background levels at ~6-6.5 ka BP. Mo/Al ratios in core ME0318 (no data are presented for Mo/Al in core EZ17G5 as Mo concentrations were below the detection limit) show a similar trend to

U/Al ratios, with ratios that are persistently elevated relative to average shale. For both cores, Mn/Al ratios show a large peak at ~10.2 ka BP, with smaller peaks at ~6 ka BP.

4.2. Benthic foraminifera

The number of benthic foraminifera (individuals per g dry sediment) is high in EZ17G5 between 10.2 and 9.6 ka BP (up to >700 ind. g^{-1}) before an abrupt disappearance at ~9.6 ka BP (BFN = 0 ind. g^{-1}, Figure 4). At ~7.8 ka BP, benthic foraminifera re-appear in small numbers until ~6.7 ka BP, after which there is a slight increase (Figure 4). A peak in BFN occurs in ME0318 between 10.2-9.8 kyr BP (>400 ind. g^{-1}). At 9.7 ka BP, there is a sharp drop in BFN which coincides with the peak in V/Al (Figure 3). Subsequently, a second, smaller peak can be seen in the BFN from 9.7-9.5 kyr BP. From 9.5-8.6 kyr BP very few benthic foraminifera were found. There are two periods, between ~8.6-8.1 kyr BP and 7.5-6.6 kyr BP, where there were no BFN in ME0318. Those two periods were interrupted by an interval of ~500 years (8.0-7.5 kyr BP) with very low numbers of benthic foraminifera. After ~6.6 ka BP, the number of benthic foraminifera increases slowly.

The calculated diversity and oxygen indices for both sediment cores show some differences between the sampling locations (Figure 4). In EZ17G5, both indices begin to decline at ~11 kyr BP and this continues until ~9.6 kyr BP, followed by an abrupt drop to zero. At about 7.9 ka BP, there is a short-lived peak in both indices, followed by an overall slow, but fluctuating, recovery. At ~6.4 ka BP, diversity reaches a relatively constant value of H(S) = ~2, while OI is steady at ~0.7. In ME0318, diversity shows an overall decrease from 10.5-8.8 kyr BP, after which no benthic foraminifera were found until a depth of ~112 cm in the core. The OI shows a similar overall trend, but with a small increase between 9.3-8.8 kyr BP. From ~8.1-7.6 kyr BP, there is a sharp increase in both diversity and OI, followed by a return to zero in both parameters, and then a rise to relatively constant levels after ~6.5 ka BP.

4.3. Iron speciation

The concentrations of Fe in different extraction phases are shown in Figure 5. The $Fe(III)_{unsulf}$ and $Fe(III)_{ox1}$ pools, dominantly comprising surface reduced Fe(II) and hydrous ferric oxides (e.g., ferrihydrite), respectively, are present at low concentrations in both cores, although there is some suggestion of an overall decrease with time for these fractions in the deeper water ME0318 core. Both the Fe_{ox} (dominantly comprising crystalline Fe (oxyhydr)oxides) and Fe_{mag} pools show distinct decreases from ~10.2-6 kyr BP, which essentially mirrors an opposite trend in Fe_{sul} (comprising Fe in pyrite and acid volatile sulfides). However, there is also a distinct peak in Fe_{sul} in both cores from ~10.2-9.5 kyr BP.

Fe_T/Al shows clear peaks in both cores between ~10.2-9.5 kyr BP (Figure 3), approximately coincident with peaks in the number of low-oxygen adapted benthic foraminifera (Figure 4), V/Al ratios (Figure 3)

and Fe_{sul} (Figure 5). Fe_T/Al ratios then fluctuate around a lower average value until ~6.3 ka BP, after which more stable low values occur (Figure 3), although Fe_T/Al ratios are persistently elevated relative to average shale (average shale Fe_T/Al = 0.59, Turekian and Wedephol, 1961), consistent with high total Fe in sediments transported by the Nile river (Poulton and Raiswell, 2002). The initial peaks in Fe_T/Al in both cores are matched by coincident peaks in Fe_{HR}/Fe_T, and Fe_{HR}/Fe_T ratios then gradually decline in both cores, although values remain elevated (above 0.38) for longer in the deeper water ME0318 core (Figure 6). Similarly, Fe_{sul}/Fe_{HR} ratios show an initial peak before ~9.5 ka BP, and ratios then decrease gradually until a more rapid drop at ~6.3 ka BP (Figure 6). However, Fe_{sul}/Fe_{HR} ratios rarely reach the lower threshold for possible identification of euxinic water column conditions in the Eastern Mediterranean (Benkovitz et al., 2020), and never exceed the more conservative threshold for robust identification of water column euxinia of >0.8 (Poulton and Canfield, 2011).

4.4. Phosphorus speciation

In core EZ17G5, total P (P_T) increases from ~18.8 μmoles/g prior to the start of S1 sapropel deposition at 10.2 ka BP, to a maximum at ~9.6 ka BP, followed by a slow overall decrease to background concentrations after ~6 ka BP (Figure 7). P_{org} increases from background levels before ~10.2 ka BP, to a peak of 2.77 μmoles/g at ~9ka BP. There was then a decrease to a minimum during the ~8.2 ka BP interruption (Figure 7), followed by a smaller increase before decreasing to background levels at ~6 ka BP. P_{aut} closely mirrors the P_T trend, with an increase from ~8.2 μmoles/g before ~10.2 ka BP to a maximum of 17.3 μmoles/g, followed by a slow decrease to a minimum of 7.0 μmoles/g. The P_{Fe} profile is approximately the inverse of P_{aut}, with a high of 3.4 μmoles/g before ~10.2 ka BP, a decrease to an average of 2.9 μmoles/g up to ~8.2 ka BP, followed by a gradual increase before reaching a relatively constant background value after ~6 ka BP. In contrast to the other P species, P_{det} is highest before ~10.2 ka BP (5.66 μmolesP/g), and decreases steadily to an approximately constant value of 2.9-3.1 μmoles/g from ~6 ka BP onwards.

The P speciation trends in core ME0318 are similar to those in core EZ17G5, but less well defined (Figure 7). Total P varies considerably, but is generally higher in the interval from ~10.2-6 kyr BP, with a pronounced peak from ~8.2-7.5 kyr BP. P_{org} also varies considerably, with a pronounced peak at ~10 ka BP. P_{aut} increases from 13.5 μmoles/g prior to 10.2 ka BP, to an average value of 18.7 μmoles/g and a peak value of 29.4 μmoles/g at ~7.8 ka BP. There is then a steady overall decrease to background values after ~6 ka BP. P_{Fe} initially decreases from background values before 10.2 ka BP, to an average of 2.4 μmoles/g, followed by a gradual increase after ~8.2 ka BP. P_{ads} shows a very similar trend to core EZ17G5, with particularly low values from ~10.2-6 kyr BP. P_{det} shows a gradual decrease from values of ~4.4 μmoles/g before ~10.2 ka BP, to relatively constant concentrations of 3.8–4 μmoles/g after ~6 ka BP.

5. DISCUSSION

5.1. Timing of sapropel deposition

Sapropels are defined by increases in Ba/Al and/or TOC, as indicators of higher productivity and preservation (De Lange et al., 2008). In both cores, Ba/Al and TOC show a marked increase from background levels starting at ~10.2 ka BP (Figure 3), which denotes the start of S1 sapropelic conditions. Both Ba/Al and TOC show a more protracted decrease to background levels, placing the termination of sapropel S1 deposition at ~6 ka BP, although this is more poorly defined than the onset (Figure 3). These ages are compatible with the range of ages given for the start (9770 ± 350 ka BP) and end (5710 ± 440 ka BP) of sapropel SI formation (De Lange et al., 2008).

5.2. Redox state of the water column

Our understanding of the redox state of the water column during sapropel S1 deposition has become more nuanced over recent years. It now appears there was a 4 layer water mass structure in the EMS in general, and the S.E. Levantine basin in particular, during this period (Zirks et al., 2019). The upper 500 m was similar to the present water mass structure with two water mass layers (Myers and Rohling, 2000) and was likely oxygenated, while the deep water beneath 1800 m was stagnant and euxinic (De Lange et al., 2008; Azrieli-Tal et al., 2014). Between 500 and 1800 m the SIW was intermittently ventilated (Grimm et al., 2015; Zirks et al., 2019).

Our approach of combining benthic species data with RSTM and Fe speciation, allows a particularly detailed reconstruction of water column redox dynamics across a mid-depth range at the heart of SIW (1200-1430 m), which we subsequently consider in relation to previous studies of shallower and deeper settings. We find no evidence for euxinic water column conditions in SIW, since samples with elevated Fe_{HR}/Fe_T (>0.38) have Fe_{sul}/Fe_{HR} ratios that fall below thresholds for identifying euxinia (Figure 6). We provide support for this by considering covariation between Mo and U enrichment factors (EF) (Figure 8), which were calculated relative to average shale (Turekian and Wedepohl, 1961). Samples from both cores plot close to the particle shuttle zone (Algeo and Tribovillard, 2009; Tribovillard et al., 2012), which suggests that relative Mo enrichments (Figure 3) likely occurred due to drawdown of Mo in association with Fe-Mn (oxyhydr)oxide minerals, rather than the development of euxinia (Algeo and Tribovillard, 2009; Tribovillard et al., 2012), although the development of sulfidic porewaters may have helped retain Mo in the sediment (Scholz et al., 2011).

However, the combined data show significant temporal variability in the intensity of oxygen depletion, which we discuss in detail below and summarise in Figures 3-6. Based on some samples with moderate Mo concentrations during sapropel S1 deposition at 1022 m water depth, Zwiep et al.

(2018) suggest that the water column may have been intermittently euxinic. While this is a possibility, the MoEF vs UEF systematics we observe (Figure 8), coupled with our detailed Fe speciation data, suggest that it was more likely that the water column was not intermittently euxinic (or only very rarely so), and instead Mo was dominantly brought down to the sediment in association with the high concentrations of Fe (oxyhydr)oxide minerals supplied to the EMS by the Nile river (Poulton and Raiswell, 2002).

Benthic foraminifera species, grouped into epifaunal, shallow infaunal and deep infaunal forms are shown for core EZ17G5 (Figure S1), core ME0318 (Figure S2) and SL112 (Figure S3). Some species are able to tolerate very low amounts of oxygen (Sen Gupta and Machain-Castillo, 1993) and are even able to respire nitrate through denitrification (Risgaard-Petersen et al., 2006; Høgslund et al., 2008; Piña-Ochoa et al., 2009). The different groups generally indicate different oxygen and food levels (Jorissen et al., 1995; de Stigter, 1996). At the sediment-water interface, epifaunal species live under well-oxygenated conditions and can survive under reduced food supply (oligotrophic conditions). Under mesotrophic conditions, food supply is increased and oxygen starts to decrease, this still favours epifaunal species, but shallow infaunal species numbers increase. Under eutrophic conditions (high food supply, low oxygen), deep infaunal species are the dominant forms that can migrate up to the sediment-water interface (de Stigter, 1996). Following the microhabitat descriptions of den Dulk et al. (1998), Kaiho (1994), Sen Gupta and Machain-Castillo (1993), and Van Der Zwaan et al. (1999), the benthic foraminifera species discussed here are categorized by their adaptation to different oxygen levels (Table 1).

In both of the cores analysed in the present study, we find that oxygenated water column conditions persisted until ~10.2 ka BP, which is supported by analyses of core SL112 at 892 m (Kuhnt, 2008). This interpretation is based on the presence of miliolid species which require a well-ventilated water column, and on the high percentages of *H. elegans*, *C. pachyderma* and *C. carinata,* which imply an increased carbon supply but also well-ventilated conditions (Table 1; Figures S1-S3). At the same time, a decreasing trend occurs in the OI, diversity remains relatively constant in the deeper ME0318 core (although there is a slight decrease in the shallower EZ17G5 core; Figure 4), TOC and RSTM concentrations are low (Figure 3), and Fe_{HR}/Fe_T ratios (<0.38) do not show evidence for deposition from an anoxic water column (Figure 6). Taken together, these observations suggest a gradual decrease in the oxygen content of the water column prior to the onset of sapropel deposition at ~10.2 ka BP.

There is a short period of time (~10.2-9.8 kyr BP in ME0318; ~10.2-9.6 kyr BP in EZ17G5) where the number of benthic foraminifera show a major increase (Figure 4). A similar increase was also observed in core SL112 (Kuhnt, 2008), while Zwiep et al. (2018) find evidence for increased primary productivity based on dinocyst accumulation rates. The diversity in this period varies around 2 and the OI is below

0.4. The high peak in BFN in all three cores consisted of *C. pachyderma, B. variabilis*, *Bulimina* spp., *Brizalina* spp., *Fursenkoina* spp., *C. bradyi*, *C. oolina* and *Globobulimina* spp. (see Figures S1-S3). *C pachydermus* and *B. variabilis* are 'transition' species that can tolerate reduced oxygen levels, but cannot survive anoxic conditions (Sen Gupta and Machain-Castillo, 1993; Kaiho, 1994). These species also suggest an increased flux of organic matter (Sen Gupta and Machain-Castillo, 1993; Kaiho, 1994), which is evident in Figure 3. The occurrence of *Bulimina* spp. and *Brizalina* spp. together indicate stronger stratification of the water mass (Kaminski et al., 2002). *Fursenkoina* spp., *Globobulimina* spp., *C. bradyi* and *C. oolina* also indicate lower amounts of oxygen and increased organic matter availability (Corliss, 1985; Mackensen and Douglas, 1989; Kaiho, 1994; den Dulk et al., 1998; de Stigter et al., 1998; De Rijk et al., 2000; Kaminski et al., 2002).

At this depth interval (120 cm; 10.2 ka BP), U/Al ratios begin to increase, but V/Al ratios remain low (Figure 3), while Fe_T/Al, Fe_{HR}/Fe_T and Fe_{sul}/Fe_{HR} all begin to increase. Enrichments in Fe_T/Al and Fe_{HR}/Fe_T (and indeed some trace metals) at the base of the sapropel could arise through mobilization during diagenesis beneath the sapropel, followed by upwards diffusion. However, the coherent behavior we document between Fe-S and RSTM systematics, coupled with benthic foraminifera indices, suggests that such a process is unlikely to be the dominant reason for the observed enrichments in Fe_T/Al and Fe_{HR}/Fe_T, which persist for some time through the sapropel. Indeed, this occurs despite the development of sulfidic porewaters (as indicated by Fe_{py}/Fe_{HR} ratios) beneath the sapropel, which would act to restrict mobilization of Fe^{2+} through precipitation of Fe sulfides. Thus, we invoke a dominant water column source for Fe enrichments, which could potentially arise in a variety of ways, including from dissolved Fe(II) released in deeper anoxic waters, followed by oxidation and sedimentation under dysoxic conditions. Alternatively, Fe enrichments may also occur directly following release of Fe(II) from sediments under dysoxic OMZ-like conditions (Scholz, 2018), or the source of Fe could have been from shallower settings, since Zirks et al. (2019) noted that anoxic conditions had already developed at a depth of ~550 m (core PS009PC; Hennekam et al. 2015). Whatever the source of Fe, the increased sulfidation of Fe phases (Figure 6) was likely due to diagenetic pyrite formation, since throughout the core, an increased prevalence of sulfidized Fe minerals (e.g., pyrite) occurs at the expense of crystalline Fe (oxyhydr)oxides (Figure 5). These combined observations are consistent with progressive depletion of oxygen from the water column across this interval.

There is then a major peak in V/Al in both cores at ~9.8 ka BP (possibly occurring slightly earlier in core ME0318), which coincides with high U/Al in core EZ17G5 and increasing U/Al in core ME0318 (Figure 3), as well as peaks in Fe_{HR}/Fe_T (Figure 6). At this time, BFN, diversity and OI drop to zero in core EZ17G5 and there is a dramatic, but short-lived, decrease in these parameters in core ME0318. This interval thus appears to represent the onset of fully anoxic water column conditions, with a return to lower V/Al following the initial drawdown pulse. Thus, the enrichments we observe in Fe_{HR}/Fe_T across this

interval most likely reflect the development of ferruginous water column conditions, rather than Fe^{2+} mobilization and subsequent precipitation under nitrogenous OMZ conditions (c.f., Scholz, 2018), but the most significant point is the development of anoxic, non-sulfidic conditions at this time.

This interval of apparent water column anoxia coincides with a period of increased Nile flow, reduced surface salinity caused by the Nile flood plume, and increased nutrient supply and primary productivity, which is characteristic of the early stages of sapropel S1 deposition (Mojtahid et al., 2015). Anoxic conditions persisted until at least 8.2 ka BP in core EZ17G5. The situation is less clear in core ME0318, but low and fluctuating BFN, diversity and OI, coupled with intermediate U/Al likely suggest a return to dysoxic conditions, before full anoxia was re-established from ~8.6-8.2 kyr BP. However, it should be noted that the foraminifera data are based on very few individuals and thus their reliability is uncertain.

An interruption of anoxic conditions at ~8.2 ka BP, coincident with a global cooling event, is a characteristic of all sediment cores deposited in the EMS between 500-1800 m (Rohling et al., 1997; Myers and Rohling, 2000; Mojtahid et al., 2015; Zwiep et al., 2018; Zirks et al., 2019). This global cooling event caused partial reventilation of SIW (Zirks et al., 2019), as well as a decrease in the magnitude of the river Nile flood (Rohling and Pälike, 2005). In ME0318, there is an indication of a slight drop in TOC and Ba/Al (Figure 3), while the main foraminifera species that occur during the interruption are various *miliolids*, the opportunistic species *A. tubulosa,* and deep infaunal species such as *Fursenkoina* spp., *Globobulimina* spp., *C. bradyi* and *C. oolina* (Figure S2). This combination of species that prefer different habitats may indicate fluctuating low oxygen levels on time scales shorter than the sample resolution of one centimeter. In EZ17G5 the interruption is observed by a more distinct drop in Ba/Al and TOC (Figure 3), but coincides with little change (or potentially a delayed change) in the benthic foraminifera record (Figure 4). The ventilation episode is dominated by *Bulimina* spp. in core SL112, which implies high organic carbon content and dysoxic conditions (den Dulk et al., 1998; de Stigter et al., 1998; Licari and Mackensen, 2005). During the same period at EZ17G5, there was a minor decrease in Fe_{HR}/Fe_T (Figure 6), supporting partial reventilation of the water column.

After the partial re-oxygenation interruption there was a second period of anoxia, but the persistence of anoxia varied as a function of water depth. The Nile runoff was less intense and there was a lower increase in PP compared with S1a (Mojtahid et al., 2015) In the shallower core EZ17G5 (and in core SL112 at 892 m), anoxia was short-lived and benthic foraminifera re-appeared gradually until the post S1 fauna was established at ~6.5-6.0 kyr BP (Figure 4). In EZ17G5, the first species to return were low-oxygen forms such as *Fursenkoina* spp., but also shallow infaunal *Uvigerina* spp. and epifaunal *G. orbicularis*. This may indicate that the water column was poised between very low and moderate oxygen conditions. In SL112, the re-colonizing species were shallow infaunal (*Uvigerina* spp.) and

epifaunal (*G. orbicularis*), rather than deep infaunal (Kuhnt, 2008). *Uvigerina* spp. comprised two species, *U. mediterranea* and *U. peregrina* in both EZ17G5 and ME0318, but the more common species was *U. peregrina* before and after sapropel S1*. U. peregrina* tolerates moderate oxygen conditions and responds to seasonal input of fresh organic matter (Fontanier et al., 2003; Licari and Mackensen, 2005). *G. orbicularis* is an opportunistic species that needs high oxygen concentrations (Kaiho, 1994). In core EZ17G5 (1200 m), Fe_{HR}/Fe_T and Fe_{sul}/Fe_{HR} gradually decrease after the reventilation episode (Figure 6), with a return to background levels at ~6 ka BP, supporting a progressive return to more oxygenated conditions, consistent with increasing OI, diversity and BFN (Figure 4), a gradual decrease in U/Al (Figure 3), and a gradual increase in Mn/Al (which would result in the precipitation of Mn (oxyhydr)oxides; Figure 3). In ME0318, there are no BFN until ~6.4 ka BP and then the re-colonization occurs more abruptly. The full range of epifaunal (different from before S1), shallow infaunal and deep infaunal species returns, indicating normal well-oxygenated marine conditions, consistent with decreasing U/Al (Figure 3) and Fe_{HR}/Fe_T ratios (Figure 6).

5.3. Phosphorus cycling during the changing redox conditions of the evolving OMZ

Phosphorus is commonly considered the ultimate limiting nutrient on geological timescales (Tyrrell, 1999). Sediments represent the location where P can be recycled back to the ocean biosphere. Sediments are also where P is ultimately lost from the biosphere by deposition and burial. These recycling and burial processes depend on the redox status of the sediment and overlying water column, because of the clear association of P with organic matter and redox-sensitive iron minerals (Van Cappellen and Ingall, 1994; Slomp et al., 2004; Tsandev et al., 2012).

At the same time as changes in the redox state of the water column, there were systematic changes in the speciation of phosphorus in the sediment. In particular, the clear decrease in P_{Fe} and P_{sorb}, along with the concomitant increase in P_{aut} in both cores (Figure 7), implies 'sink-switching', as P associated with Fe (oxyhydr)oxide minerals was released during reductive dissolution and subsequently precipitated as carbonate fluorapatite (Ruttenberg and Berner, 1993; März et al., 2014). Indeed, the gradual increase in P_{Fe} and P_{sorb}, and decrease in P_{aut}, after the 8.2 ka BP ventilation event, is consistent with less intense redox cycling of P as conditions slowly returned to pre-sapropel times.

The behaviour of organic P is, however, more complex than the other diagenetically reactive P species. The increase in P_{org} at the start of sapropel deposition in core EZ17G5, followed by the subsequent decrease at the end of sapropel deposition (Figure 7), is entirely consistent with elevated primary productivity and organic carbon burial (Figure 3). This increase in primary productivity was likely due to an enhanced nutrient influx at this time, when the Nile flood plume was substantially increased. However, with the exception of an initial peak at the onset of sapropel deposition, P_{org} remains relatively constant throughout the entire interval in the deeper ME0318 core (Figure 7), despite

elevated TOC during sapropel deposition (Figure 3). This may be due to either redox cycling and 'sink-switching' during diagenesis, or recycling of P_{org} back to the water column. These possibilities are important to evaluate as P recycling may ultimately promote additional primary productivity, hence contributing to both water column deoxygenation and elevated organic carbon burial (Slomp et al., 2004).

To provide further insight into the potential significance of P recycling we consider TOC/P_{org} and $TOC/P_{reactive}$ ratios (Figure 9). For both cores, TOC/P_{org} increases to a maximum during sapropel deposition, with values well above the Redfield ratio. This indicates preferential microbial release of P from organic matter, likely during settling through the water column and during diagenesis (Pujo-Pay et al., 2011). However, with the exception of a few samples deposited under anoxic water column conditions immediately after the 8.2 ka BP ventilation event, $TOC/P_{reactive}$ ratios fall below the canonical Redfield ratio for living marine phytoplankton of 106:1, implying significant trapping of P in authigenic phases. Indeed, the increase in P_{aut} concentrations during sapropel deposition is far higher than the combined decrease observed in P_{Fe} and P_{sorb} (Figure 7), implying significant trapping of P_{org} in authigenic phases during diagenesis. It should also be noted, however, that reactive P would also originally have been augmented by sequestration of P in association with Fe (oxyhydr)oxide minerals, which would lower primary $TOC/P_{reactive}$ ratios relative to the Redfield ratio. Thus we cannot rule out the possibility of a limited degree of P recycling back to the water column during diagenesis, in addition to the recycling that would have occurred during particle settling through the water column.

Slomp et al. (2004) calculated the flux of phosphate into the overlying water from sediments deposited in the deeper euxinic basin during S1 sapropel deposition, and speculated that this recycled phosphate would increase primary productivity in the basin if it reached the photic zone. Slomp et al. (2004) were unable to carry out a similar calculation in their SIW depth cores as it was not possible to quantitatively determine the burial efficiency of TOC or P. Similarly, we are unable to quantitively constrain the possible extent of P recycling from our cores. Based on the 4 layer water column structure (see Figure 10) proposed during S1 deposition (Zirks et al., 2019), whatever phosphate was recycled would initially be recycled into the SIW (500-1800 m), and from there into the base of the Levantine intermediate water (200-500 m). As occurs at present, once mixed into the LIW, recycled P would have been fluxed out of the basin (Powley et al., 2016). However, we suggest that this study represents a possible template for modern evolving OMZs. In those situations where the recycled P is upwelled into the photic zone, these recycling P processes represent an important positive feedback mechanism.

In contrast to the other P species, the concentration of P_{det} was not directly affected by the oxygen status of the overlying water. Instead, the systematic decrease in P_{det} from the bottom of the core until the ventilation event, followed by roughly constant concentrations after (Figure 7), is similar to

changes in external detrital input of Blue Nile sediment and/or Saharan dust input observed previously at core 9509, a location close to the present Israeli coast and also under the Sapropel Nile flood plume (Box et al., 2011). These changes have been interpreted as being due to the effects of the African Humid Period, which reduced soil erosion in the Ethiopian Highlands (the source of the Blue Nile) and dust production from what is now the Sahara desert. Given that P_{det} in modern Blue Nile sediment is 9.9 μmoles/g, while the content from Saharan dust is 3.3 μmoles/g (Eijsink et al., 2000), it is likely that most of the observed increase in P_{det} with depth was a result of increased Blue Nile input, which is consistent with the suggestion of an elevated P influx (as dissolved, particulate reactive and detrital) at the height of the Nile flood. Based on this observation, combined with our evaluation of the limited significance of P recycling, we conclude that the dominant factor driving deoxygenation in this part of the Eastern Mediterranean Levantine basin was an enhanced nutrient influx at the maximum of the Nile flood. Indeed, the gradual decrease observed in P_{det} through sapropel S1 (Figure 7) is consistent with a progressive decrease in nutrient inputs from the Nile flood, which appears to have resulted in a gradual recovery from anoxia, as indicated by generally less extreme oxygen depletion after the 8.2 ka BP ventilation event (Figures 3-6).

5.4. Evolution of the S.E. Levantine basin water column

Based on the spatial and temporal changes in redox conditions we document, it is possible to develop a dynamic model of the growth and development of the intermediate depth OMZ in the S.E. Levantine basin during the early Holocene (Figure 10). In relating this model to modern and future OMZs, we recognise that some OMZs may be more likely to be characterized by the generation of water column sulfide as oxygen depletion progresses to full anoxia (Scholz, 2018). However, we also note that enhanced chemical weathering under a warming climate would promote an increased oceanic influx of Fe_{HR} over sulfate, due to additional release of Fe from silicate minerals (Poulton and Raiswell, 2002), and this would greatly enhance the likelihood for future development of anoxic, non-sulfidic conditions in OMZs (Poulton and Canfield, 2011). Thus, we consider the S.E. Levantine basin during the early Holocene to be a prime model for the progressive development of a significant proportion of modern OMZs, as they potentially transition to a fully anoxic state.

In the S.E. Levantine basin, there was a fully oxygenated water column prior to the Holocene (Schmiedl et al., 2010). Starting at ~10.2 ka BP, oxygen decreased in the water column and sapropel deposition started initially in shallow water (>500 m) and later at greater depth (Zirks et al., 2019), as is characteristic of oxygen depletion in modern OMZ settings (Levin, 2003). Thus, the water column was already anoxic at 500-900 m between ~10.2-9.8 kyr BP (Hennekam et al., 2015; Zirks et al., 2019), below this depth (at 1200 m and 1430 m) oxygen was depleted, but the water column was not yet anoxic. Between 9.8-8.2 kyr BP, the OMZ expanded until the entire water column below ~500 m

eventually became anoxic by ~8.6 ka BP. The results from this study and Matthews et al. (2017) suggest that, when anoxic, the intermediate water column between 500 and 1800 m was not euxinic. During the 8.2 ka interruption the intermediate water column became dysoxic, as a result of increased water mass formation caused by fluctuating natural climate change and thus increased water mass flow towards the east. After the ventilation event, oxygen levels deteriorated again, with an initial short-lived development of anoxic conditions, but with a gradual recovery to pre-sapropel conditions by ~6 ka BP.

These changes in the oxygen status of SIW suggest that after the reventilation episode at ~8.2 ka BP, shallower water settings recovered more rapidly than deeper water settings, whereas oxygen depletion was possibly more intense in shallower water settings prior to the reventilation episode, suggesting that shallower water settings exerted the initial control on both the onset and termination of oxygen depletion. However, the redox dynamics that are evident in SIW contrast with the deepest waters in the S.E. Levantine basin, which remained stagnant and euxinic throughout the period of sapropel S1, based on both RSTM and Fe speciation (De Lange et al., 2008; Azrieli-Tal et al., 2014; Matthews et al., 2017). Furthermore, in contrast to SIW, there was synchronous formation of euxinic conditions in the deep water and reventilation (De Lange et al., 2008). Such differences are possible if, in parallel to the modern situation, the location of deep water and intermediate water formation in the EMS were widely seperated and responded to somewhat different physical forcings.

5.5 Implications for modern systems

The pattern for the evolution of the S.E. Levantine basin OMZ during deposition of sapropel SI provides a template for possible modern climate and environmental change into the future. In the modern ocean, reduced oxygen levels are expanding in two situations in particular – in open ocean OMZs and in hypoxic areas on the shelf close to the outflow of major rivers. Oxygen minimum zones are specifically expanding in oceanic intermediate waters, such as in the east central Pacific, eastern N. Atlantic and the Indian Ocean (Stramma et al., 2008). In many of these cases, the expansion is interpreted as being due to increasing temperature resulting in decreased oxygen solubility (Keeling et al., 2010) and changes in ocean circulation patterns and biogeochemical feedback mechanisms (Oschlies et al., 2008), although it is also possible that increased anthropogenic nutrient inputs may be increasing primary productivity and labile carbon export (Ito et al., 2016).

The seasonal hypoxic areas that occur adjacent to many modern major rivers (Li et al., 2002; Duan et al., 2008; Shi and Wang, 2009; Satpathy et al., 2013; Kolker et al., 2014) are commonly caused by increased anthropogenic nutrient supply. Although there is evidence that these hypoxic zones are expanding, there is no evidence yet, except possibly in the Bay of Bengal, that these oxygen depleted zones have spread into adjacent intermediate waters. In no cases have modern OMZs yet become

anoxic or even ferruginous, although there has been an observed increase in dissolve Fe in the north east Atlantic (Klar et al., 2018).

Natural climate change was the ultimate cause of the evolving OMZ in offshore intermediate waters observed in the present study. The immediate cause of the expanding OMZ was a slowing of water mass formation interacting with increased nutrient supply from the plume of a major river (Zirks et al., 2019). As with the present day, the temperature of the water column increased (by 3-4°C) from the end of the glacial period until the beginning of sapropel S1 (Castañeda et al., 2010), causing a decrease in the oxygen carrying capacity of the intermediate water. It is likely that if the deoxygenation of modern oceanic OMZs continues, some settings may evolve to anoxia with increased solubility of Fe in the water column, as long as there is sufficient supply of labile Fe, which could be from atmospheric dust and/or river particulates. This has already been observed in a modern OMZ (Klar et al., 2018). Similarly, if the deoxygenation of water on the shelf adjacent to large rivers continues, then it is likely that such areas will develop from hypoxic patches to full anoxia. In such situations there may be a positive feedback caused by enhanced P recycling due to anoxia in the overlying water, as has been observed during past periods of ocean anoxia (Jenkyns, 2010).

It is recognized, however, that although all oceanic systems subject to increased labile carbon input and limited reventilation will evolve through a classic sequence of biogeochemical change (e.g., Froelich et al., 1979), not all will remain poised at the precise redox state observed in the EMS during Sapropel S1 deposition, where the SIW remained anoxic and non-sulfidic for several thousand years. Indeed, some systems may evolve to the more extreme state of euxinia, which may be particularly likely in settings that do not receive a high supply of Fe (oxyhydr)oxide minerals from major river systems. It is also worth noting that restricted euxinic systems such as the modern Black Sea have a much thinner anoxic non-sulfidic zone because of a sharp boundary between ventilated surface waters and stagnant saline waters, which is controlled by the rate of export carbon and the ventilation rate of the water overlying the stagnant deep water (e.g., Konovalov et al., 2006).

In this regard, the development of a major zone of anoxic, non-sulfidic water column conditions in the SIW of the EMS was related to a number of factors. The present deep water in the EMS has a low nitrate content because of its anti-estuarine circulation and short water residence time (Krom et al., 2013). During sapropel deposition, the circulation in the upper 500 m was also anti-estuarine, although the rate of water exchange was probably slower (Zirks et al., 2019), and this promoted the development of anoxic non-sulfidic, rather than nitrogenous, conditions. In addition, there was likely to have been a higher input of Fe (oxyhyr)oxides from the increased Nile flood (Poulton and Raiswell, 2002), which would have helped poise the system in an anoxic, non-sulfidic state (Poulton and Canfield, 2011). Even under these conditions, however, the system was reset due to a change in water

ventilation rates during the 8.2 ky climatic event. In the case of the S.E. Levantine basin during sapropel S1 deposition, oxygen depletion was only permanently reversed when natural climate change resulted in the end of the African Humid period, which reduced the Nile flood plume and its load of bioavailable nutrients to modern values.

Acknowledgments:

The authors would like to express appreciation to support received from Sir Mick Davis (BNGT) and Mr. Norman Kirscher (BNGT) for academic scholarship funding (EZ). The research did not receive any specific grant from funding agencies in the public commercial or not-for-profit sectors. SWP acknowledges support from a Royal Society Wolfson Research Merit Award. This manuscript was completed as our respective countries went into lock down caused by the corona virus.

References

Algeo T. J. and Tribovillard N. (2009) Environmental analysis of paleoceanographic systems based on molybdenum–uranium covariation. *Chem. Geol.* **268**, 211–225.

Anderson R. F., Fleisher M. Q. and LeHuray A. P. (1989) Concentration, oxidation state, and particulate flux of uranium in the Black Sea. *Geochim. Cosmochim. Acta* **53**, 2215–2224.

Azrieli-Tal I., Matthews A., Bar-Matthews M., Almogi-Labin A., Vance D., Archer C. and Teutsch N. (2014) Evidence from molybdenum and iron isotopes and molybdenum–uranium covariation for sulphidic bottom waters during Eastern Mediterranean sapropel S1 formation. *Earth Planet. Sci. Lett.* **393**, 231–242. Available at: http://linkinghub.elsevier.com/retrieve/pii/S0012821X14001411.

Benkovitz A., Matthews A., Teutsch N., Poulton S. W., Bar-Matthews M. and Almogi-Labin A. Tracing water column euxinia in eastern Mediterranean sapropels S5 and S7. *Chem. Geol.*

Bertine K. K. and Turekian K. K. (1973) Molybdenum in marine deposits. *Geochim. Cosmochim. Acta* **37**, 1415–1434.

Box M. R., Krom M. D., Cliff R. A., Bar-Matthews M., Almogi-Labin A., Ayalon A. and Paterne M.

(2011) Response of the Nile and its catchment to millennial-scale climatic change since the LGM from Sr isotopes and major elements of East Mediterranean sediments. *Quat. Sci. Rev.* **30**, 431–442. Available at: http://dx.doi.org/10.1016/j.quascirev.2010.12.005.

Breitburg D., Levin L. A., Oschlies A., Gregoire M., Chavez F. P., Conley D. J., Garcon V., Gilbert D., Gutierrez D., Isensee K., Jacinto G. S., Limburg K. E., Montes I., Naqvi S. W. A., Pitcher G. C., Rabalais N. N., Roman M. R., Rose K. A., Seibel B. A., Telszewski M., Yasuhara M. and Zhang J. (2018) Declining oxygen in the global ocean and coastal waters. *Science (80-.).* **359**, 1–11.

Buzas M. A. and Gibson T. G. (1969) Species Diversity: Benthonic Foraminifera in Western North Atlantic. *Science (80-.).* **163**, 72–75.

Canfield D. E., Raiswell R. and Bottrell S. H. (1992) The reactivity of sedimentary iron minerals toward sulfide. *Am. J. Sci.* **292**, 659–683.

Canfield D. E., Raiswell R., Westrich J. T., Reaves C. M. and Berner R. A. (1986) The use of chromium reduction in the analysis of reduced inorganic sulfur in sediments and shales. *Chem. Geol.* **54**, 149–155. Available at: http://www.sciencedirect.com/science/article/pii/0009254186900781.

Van Cappellen P. and Ingall E. D. (1994) Benthic phosphorus regeneration, net primary production, and ocean anoxia: a model of the coupled marine biogeochemical cycles of carbon and phosphorus. *Paleoceanography* **9**, 677–692.

Castañeda I. S., Schefuß E., Pätzold J., Sinninghe Damsté J. S., Weldeab S. and Schouten S. (2010) Millennial-scale sea surface temperature changes in the eastern Mediterranean (Nile River Delta region) over the last 27,000 years. *Paleoceanography* **25**, 1–13.

Corliss B. H. (1985) Microhabitats of benthic foraminifera within deep-sea sediments. *Nature* **314**, 435–438.

DeMenocal P. B., Ortiz J., Guilderson T. P., Adkins J., Sarnthein M., Baker L. and Yarusinsky M. (2000) Abrupt onset and termination of the African Humid Period: Rapid climate responses to gradual insolation forcing. *Quat. Sci. Rev.* **19**, 347–361.

Diaz R. J. and Rosenberg R. (2008) Spreading dead zones and consequences for marine ecosystems. *Science (80-.).* **321**, 926–929. Available at: http://www.ncbi.nlm.nih.gov/pubmed/18703733.

Duan S., Liang T., Zhang S., Wang L., Zhang X. and Chen X. (2008) Seasonal changes in nitrogen and phosphorus transport in the lower Changjiang River before the construction of the Three Gorges Dam. *Estuar. Coast. Shelf Sci.* **79**, 239–250.

den Dulk M., Reichart G.-J., Memon G. M., Roelofs E. M. P., Zachariasse W. J. and Van Der Zwaan G. J.

693 (1998) Benthic foraminiferal response to variations in surface water productivity and
694 oxygenation in the northern Arabian Sea. *Mar. Micropaleontol.* **35**, 43–66.

695 Eijsink L. M., Krom M. D. and Herut B. (2000) Speciation and burial flux of phosphorus in the surface
696 sediments of the Eastern Mediterranean. *Am. J. Sci.* **300**, 483–503.

697 Emeis K.-C., Robertson A. H. F. and Richter C. (1996) 2. Paleoceanography and sapropel indroduction.
698 *Proc. Ocean Drill. Progr.* **160**, 21–28.

699 Emerson S. R. and Huested S. S. (1991) Ocean anoxia and the concentrations of molybdenum and
700 vanadium in seawater. *Mar. Chem.* **34**, 177–196.

701 Erickson B. E. and Helz G. R. (2000) Molybdenum(VI) speciation in sulfidic waters: Stability and lability
702 of thiomolybdates. *Geochim. Cosmochim. Acta* **64**, 1149–1158.

703 Fontanier C., Jorissen F. J., Chaillou G., David C., Anschutz P. and Lafon V. (2003) Seasonal and
704 interannual variability of benthic foraminiferal faunas at 550 m depth in the Bay of Biscay. *Deep.*
705 *Res. Part I* **50**, 457–494.

706 Froelich P., Klinkhammer G. P., Bender M. L., Luedtke N. A., Heath G. R., Cullen D., Dauphin P.,
707 Hammond D., Hartman B. and Maynard V. (1979) Early oxidation of organic matter in pelagic
708 sediments of the eastern equatorial Atlantic: suboxic diagenesis. *Geochim. Cosmochim. Acta* **43**,
709 1075–1090.

710 Goldberg T., Archer C., Vance D., Thamdrup B., McAnena A. and Poulton S. W. (2012) Controls on Mo
711 isotope fractionations in a Mn-rich anoxic marine sediment, Gullmar Fjord, Sweden. *Chem.*
712 *Geol.* **296**–**297**, 73–82. Available at: http://dx.doi.org/10.1016/j.chemgeo.2011.12.020.

713 Grimm R., Maier-Reimer E., Mikolajewicz U., Schmiedl G., Müller-Navarra K., Adloff F., Grant K. M.,
714 Ziegler M., Lourens L. J. and Emeis K.-C. (2015) Late glacial initiation of Holocene eastern
715 Mediterranean sapropel formation. *Nat. Commun.* **6**, 1–12.

716 Sen Gupta B. K. and Machain-Castillo M. L. (1993) Benthic foraminifera in oxygen-poor habitats. *Mar.*
717 *Micropaleontol.* **20**, 183–201.

718 van Helmond N. A. G. M., Hennekam R., Donders T. H., Bunnik F. P. M., de Lange G. J., Brinkhuis H.
719 and Sangiorgi F. (2015) Marine productivity leads organic matter preservation in sapropel S1:
720 Palynological evidence from a core east of the Nile River outflow. *Quat. Sci. Rev.* **108**, 130–138.
721 Available at: http://dx.doi.org/10.1016/j.quascirev.2014.11.014.

722 Helz G. R., Miller C. V., Charnock J. M., Mosselmans J. F. W., Pattrick R. A. D., Garner C. D. and
723 Vaughan D. J. (1996) Mechanism of molybdenum removal from the sea and its concentration in

724 black shales: EXAFS evidence. *Geochim. Cosmochim. Acta* **60**, 3631–3642.

725 Hennekam R., Donders T. H., Zwiep K. and de Lange G. J. (2015) Integral view of Holocene
726 precipitation and vegetation changes in the Nile catchment area as inferred from its delta
727 sediments. *Quat. Sci. Rev.* **130**, 189–199.

728 Hennekam R., Jilbert T., Schnetger B. and De Lange G. J. (2014) Solar forcing of Nile discharge and
729 sapropel S1 formation in the early to middle Holocene eastern Mediterranean.
730 *Paleoceanography* **29**, 343–356.

731 Hennekam R. and de Lange G. J. (2012) X-ray fluorescence core scanning of wet marine sediments:
732 methods to improve quality and reproducibility of high-resolution paleoenvironmental records.
733 *Limnol. Oceanogr. Methods* **10**, 991–1003. Available at:
734 http://www.aslo.org/lomethods/free/2012/0991.html.

735 Høgslund S., Revsbech N. P., Cedhagen T., Nielsen L. P. and Gallardo V. A. (2008) Denitrification,
736 nitrate turnover, and aerobic respiration by benthic foraminiferans in the oxygen minimum
737 zone off Chile. *J. Exp. Mar. Bio. Ecol.* **359**, 85–91.

738 Ito T., Nenes A., Johnson M. S., Meskhidze N. and Deutsch C. (2016) Acceleration of oxygen decline in
739 the tropical Pacific over the past decades by aerosol pollutants. *Nat. Geosci.* **9**, 443–447.

740 Jenkyns H. C. (2010) Geochemistry of oceanic anoxic events. *Geochemistry, Geophys. Geosystems* **11**,
741 Q03004.

742 Jorissen F. J. (1999) Benthic foraminiferal successions across Late Quaternary Mediterranean
743 sapropels. *Mar. Geol.* **153**, 91–101.

744 Jorissen F. J., de Stigter H. C. and Widmark J. G. V (1995) A conceptual model explaining benthic
745 foraminiferal microhabitats. *Mar. Micropaleontol.* **26**, 3–15.

746 Kaiho K. (1994) Benthic foraminiferal dissolved-oxygen index and dissolved-oxygen levels in the
747 modern ocean. *Geology* **22**, 719–722.

748 Kaminski M. A., Aksu A. E., Box M. R., Hiscott R. N., Filipescu S. and Al-Salameen M. (2002) Late
749 Glacial to Holocene benthic foraminifera in the Marmara Sea: implications for Black Sea-
750 Mediterranean Sea connections following the last deglaciation. *Mar. Geol.* **190**, 165–202.

751 Keeling R. F., Körtzinger A. and Gruber N. (2010) Ocean Deoxygenation in a Warming World. *Ann.*
752 *Rev. Mar. Sci.* **2**, 199–229.

753 Klar J. K., Schlosser C., Milton J. A., Woodward E. M. S., Lacan F., Parkinson I. J., Achterberg E. P. and
754 James R. H. (2018) Sources of dissolved iron to oxygen minimum zone waters on the Senegalese

continental margin in the tropical North Atlantic Ocean: Insights from iron isotopes. *Geochim. Cosmochim. Acta* **236**, 60–78.

Klinkhammer G. P. and Palmer M. R. (1991) Uranium in the oceans: where it goes and why. *Geochim. Cosmochim. Acta* **55**, 1799–1806.

Kolker A. S., Li C., Walker N. D., Pilley C., Ameen A. D., Boxer G., Ramatchandirane C., Ullah M. and Williams K. A. (2014) The impacts of the great Mississippi/Atchafalaya River flood on the oceanography of the Atchafalaya Shelf. *Cont. Shelf Res.* **86**, 17–33. Available at: http://dx.doi.org/10.1016/j.csr.2014.04.023.

Konovalov S. K., Murray J. W., Luther G. W. and Tebo B. M. (2006) Processes controlling the redox budget for the oxic/anoxic water column of the Black Sea. *Deep Sea Res. Part II Top. Stud. Oceanogr.* **53**, 1817–1841.

Koroleff F. (1976) Determination of nutrients. In *Methods of seawater analysis* Verlag Chemie Weinhein. pp. 117–181.

Kuhnt T. (2008) Reconstruction of Late Quaternary Deep-Sea Ecosystem Variability in the Eastern Mediterranean Sea based on Benthic Foraminiferal Faunas and Stable Isotopes. Universität Leibzig, Germany.

Kuhnt T., Schmiedl G., Ehrmann W., Hamann Y. and Andersen N. (2008) Stable isotopic composition of Holocene benthic foraminifers from the Eastern Mediterranean Sea: Past changes in productivity and deep water oxygenation. *Palaeogeogr. Palaeoclimatol. Palaeoecol.* **268**, 106–115. Available at: http://linkinghub.elsevier.com/retrieve/pii/S0031018208004148.

De Lange G. J., Thomson J., Reitz A., Slomp C. P., Speranza Principato M., Erba E. and Corselli C. (2008) Synchronous basin-wide formation and redox-controlled preservation of a Mediterranean sapropel. *Nat. Geosci.* **1**, 606–610. Available at: http://www.nature.com/doifinder/10.1038/ngeo283.

Levin L. A. (2003) Oxygen minimum zone benthos: adaptation and community response to hypoxia. *Oceanogr. Mar. Biol. an Annu. Rev.* **41**, 1–45.

Li D., Zhang J., Huang D., Wu Y. and Liang J. (2002) Oxygen depletion off the Changjiang (Yangtze River) Estuary. *Sci. China, Ser. D Earth Sci.* **45**, 1137–1146.

Licari L. and Mackensen A. (2005) Benthic foraminifera off West Africa (1°N to 32°S): Do live assemblages from the topmost sediment reliably record environmental variability? *Mar. Micropaleontol.* **55**, 205–233.

Mackensen A. and Douglas R. G. (1989) Down-core distribution o f live and dead deep-water benthic foraminifera in box cores from the Weddell Sea and the California continental borderland. *Deep. Res.* **36**, 879–900.

März C., Poulton S. W., Wagner T., Schnetger B. and Brumsack H.-J. (2014) Phosphorus burial and diagenesis in the central Bering Sea (Bowers Ridge, IODP Site U1341): perspectives on the marine P cycle. *Chem. Geol.* **363**, 270–282.

Matthews A., Azrieli-Tal I., Benkovitz A., Bar-Matthews M., Vance D., Poulton S. W., Teutsch N., Almogi-Labin A. and Archer C. (2017) Anoxic development of sapropel S1 in the Nile Fan inferred from redox sensitive proxies, Fe speciation, Fe and Mo isotopes. *Chem. Geol.* **475**, 24–39. Available at: https://doi.org/10.1016/j.chemgeo.2017.10.028.

Mojtahid M., Manceau R., Schiebel R., Hennekam R. and De Lange G. J. (2015) Thirteen thousand years of southeastern Mediterranean climate variability inferred from an integrative planktic foraminiferal-based approach. *Paleoceanography* **30**, 402–422.

Myers P. G., Haines K. and Rohling E. J. (1998) Modeling the paleocirculation of the Mediterranean: The last glacial maximum and the Holocene with emphasis on the formation of sapropel S1. *Paleoceanography* **13**, 586–606.

Myers P. G. and Rohling E. J. (2000) Modeling a 200-Yr interruption of the Holocene Sapropel S1. *Quat. Res.* **53**, 98–104.

Nameroff T. J., Balistrieri L. S. and Murray J. W. (2002) Suboxic trace metal geochemistry in the eastern tropical North Pacific. *Geochim. Cosmochim. Acta* **66**, 1139–1158.

Piña-Ochoa E., Høgslund S., Geslin E., Cedhagen T., Revsbech N. P., Nielsen L. P., Schweizer M., Jorissen F. J., Rysgaard S. and Risgaard-Petersen N. (2009) Widespread occurrence of nitrate storage and denitrification among Foraminifera and Gromiida. *Proc. Natl. Acad. Sci.* **107**, 1148–1153.

Pinardi N. and Masetti E. (2000) Variability of the large scale general circulation of the Mediterranean Sea from observations and modelling: A review. *Palaeogeogr. Palaeoclimatol. Palaeoecol.* **158**, 153–173.

Poulton S. W. and Canfield D. E. (2005) Development of a sequential extraction procedure for iron: implications for iron partitioning in continentally derived particulates. *Chem. Geol.* **214**, 209–221. Available at: http://www.sciencedirect.com/science/article/pii/S0009254104003699.

Poulton S. W. and Canfield D. E. (2011) Ferruginous conditions: A dominant feature of the ocean

through Earth's history. *Elements* **7**, 107–112.

Poulton S. W., Krom M. D. and Raiswell R. (2004) A revised scheme for the reactivity of iron (oxyhydr) oxide minerals towards dissolved sulfide. *Geochim. Cosmochim. Acta* **68**, 3703–3715.

Poulton S. W. and Raiswell R. (2002) The low-temperature geochemical cycle of iron: From continental fluxes to marine sediment deposition. *Am. J. Sci.* **302**, 774–805.

Powley H. R., Krom M. D. and Van Cappellen P. (2016) Circulation and oxygen cycling in the Mediterranean Sea: Sensitivity to future climate change. *J. Geophys. Res. Ocean.* **121**, 8230–8247.

Pujo-Pay M., Conan P., Oriol L., Cornet-Barthaux V., Falco C., Ghiglione J.-F., Goyet C., Moutin T. and Prieur L. (2011) Integrated survey of elemental stoichiometry (C, N, P) from the western to eastern Mediterranean Sea. *Biogeosciences* **8**, 883.

Raiswell R. and Canfield D. E. (1998) Sources of iron for pyrite formation in marine sediments. *Am. J. Sci.* **298**, 219–245.

De Rijk S., Jorissen F. J., Rohling E. J. and Troelstra S. R. (2000) Organic flux control on bathymetric zonation of Mediterranean benthic foraminifera. *Mar. Micropaleontol.* **40**, 151–166.

Risgaard-Petersen N., Langezaal A. M., Ingvardsen S., Schmid M. C., Jetten M. S. M., Op Den Camp H. J. M., Derksen J. W. M., Piña-Ochoa E., Eriksson S. P., Nielsen L. P., Revsbech N. P., Cedhagen T. and Van Der Zwaan G. J. (2006) Evidence for complete denitrification in a benthic foraminifer. *Nature* **443**, 93–96.

Rohling E. J., Jorissen F. J. and de Stigter H. C. (1997) 200 Year interruption of Holocene sapropel formation in the Adriatic Sea. *J. Micropalaeontology* **16**, 97–108. Available at: https://www.j-micropalaeontol.net/16/97/1997/.

Rohling E. J. and Pälike H. (2005) Centennial-scale climate cooling with a sudden cold event around 8,200 years ago. *Nature* **434**, 975–979.

Rossignol-Strick M., Nesteroff W., Olive P. and Vergnaud-Grazzini C. (1982) After the deluge: Mediterranean stagnation and sapropel formation. *Nature* **295**, 105–110.

Ruttenberg K. C. (1992) Development of a sequential extraction method for different forms of phosphorus in marine sediments. *Limnol. Oceanogr.* **37**, 1460–1482.

Ruttenberg K. C. and Berner R. A. (1993) Authigenic apatite formation and burial in sediments from non-upwelling, continental margin environments. *Geochim. Cosmochim. Acta* **57**, 991–1007.

847 Satpathy K. K., Panigrah S., Mohanty A. K., Sahu G., Achary M. S., Bramha S. N., Padhi R. K.,
848 Samantara M. K., Selvanayagam M. and Sarkar S. K. (2013) Severe oxygen depletion in the
849 shallow regions of the Bay of Bengal off Tamil Nadu coast. *Curr. Sci.* **104**, 1467–1469.

850 Schlitzer R., Roether W., Oster H., Junghans H. G., Hausmann M., Johannsen H. and Michelato A.
851 (1991) Chlorofluoromethane and oxygen in the Eastern Mediterranean. *Deep. Res.* **38**, 1531–
852 1551.

853 Schmiedl G., Kuhnt T., Ehrmann W., Emeis K.-C., Hamann Y., Kotthoff U., Dulski P. and Pross J. (2010)
854 Climatic forcing of eastern Mediterranean deep-water formation and benthic ecosystems
855 during the past 22 000 years. *Quat. Sci. Rev.* **29**, 3006–3020. Available at:
856 http://dx.doi.org/10.1016/j.quascirev.2010.07.002.

857 Schmiedl G., Mitschele A., Beck S., Emeis K.-C., Hemleben C., Schulz H., Sperling M. and Weldeab S.
858 (2003) Benthic foraminiferal record of ecosystem variability in the eastern Mediterranean Sea
859 during times of sapropel S5 and S6 deposition. *Palaeogeogr. Palaeoclimatol. Palaeoecol.* **190**,
860 139–164.

861 Scholz F. (2018) Identifying oxygen minimum zone-type biogeochemical cycling in Earth history using
862 inorganic geochemical proxies. *Earth-Science Rev.* **184**, 29–45. Available at:
863 https://doi.org/10.1016/j.earscirev.2018.08.002.

864 Scholz F., McManus J. and Sommer S. (2013) The manganese and iron shuttle in a modern euxinic
865 basin and implications for molybdenum cycling at euxinic ocean margins. *Chem. Geol.* **355**, 56–
866 68.

867 Shi W. and Wang M. (2009) Satellite observations of flood-driven Mississippi River plume in the
868 spring of 2008. *Geophys. Res. Lett.* **36**, 1–5.

869 Slomp C. P., Thomson J. and De Lange G. J. (2004) Controls on phosphorus regeneration and burial
870 during formation of eastern Mediterranean sapropels. *Mar. Geol.* **203**, 141–159.

871 de Stigter H. C. (1996) Recent and fossil benthic foraminifera in the Adriatic Sea: distribution patterns
872 in relation to organic carbon flux and oxygen concentration at the seabed. University of Utrecht.

873 de Stigter H. C., Jorissen F. J. and Van Der Zwaan G. J. (1998) Bathymetric distribution and
874 microhabitat partitioning of live (Rose Bengal stained) benthic Foraminifera along a shelf to
875 bathyal transect in the southern Adriatic Sea. *J. Foraminifer. Res.* **28**, 40–65.

876 Stookey L. L. (1970) Ferrozine - A new Spectrophotometric Reagent for Iron. *Anal. Chem.* **42**, 779–
877 781.

878 Stramma L., Johnson G. C., Sprintall J. and Mohrholz V. (2008) Expanding Oxygen-Minimum Zones in
879 the Tropical Oceans. *Science (80-.).* **320**, 655–658.

880 Stratford K., Williams R. G. and Myers P. G. (2000) Impact of the circulation on sapropel formation in
881 the eastern Mediterranean. *Gobal Biogeochem. Cycles* **14**, 683–695.

882 Stuiver M. and Reimer P. J. (1993) Extended 14C data and revised Calib 3.0 14C age calibration
883 program. *Radiocarbon* **35**, 215–230.

884 Tachikawa K., Vidal L.-A., Cornuault M., Garcia M., Pothin A., Sonzogni C., Bard E., Menot G. and
885 Revel M. (2015) Eastern Mediterranean Sea circulation inferred from the conditions of S1
886 sapropel deposition. *Clim. Past* **11**, 855–867.

887 Tribovillard N., Algeo T. J., Baudin F. and Riboulleau A. (2012) Analysis of marine environmental
888 conditions based onmolybdenum–uranium covariation—Applications to Mesozoic
889 paleoceanography. *Chem. Geol.* **324**, 46–58.

890 Tsandev I., Reed D. C. and Slomp C. P. (2012) Phosphorus diagenesis in deep-sea sediments:
891 Sensitivity to water column conditions and global scale implications. *Chem. Geol.* **330**, 127–139.

892 Turekian K. K. and Wedepohl K. H. (1961) Distribution of the elements in some major units of the
893 earth's crust. *Geol. Soc. Am. Bull.* **72**, 175–192.

894 Tyrrell T. (1999) The relative influences of nitrogen and phosphorus on oceanic primary production.
895 *Nature* **400**, 525–531.

896 Wu J., Pahnke K., Böning P., Wu L., Michard A. and de Lange G. J. (2019) Divergent Mediterranean
897 seawater circulation during Holocene sapropel formation – Reconstructed using Nd isotopes in
898 fish debris and foraminifera. *Earth Planet. Sci. Lett.* **511**, 141–153.

899 Xiong Y., Guilbaud R., Peacock C. L., Cox R. P., Canfield D. E., Krom M. D. and Poulton S. W. (2019)
900 Phosphorus cycling in Lake Cadagno, Switzerland: A low sulfate euxinic ocean analogue.
901 *Geochim. Cosmochim. Acta*.

902 Zegeye A., Bonneville S., Benning L. G., Sturm A., Fowle D. A., Jones C., Canfield D. E., Ruby C.,
903 MacLean L. C., Nomosatryo S., Crowe S. A. and Poulton S. W. (2012) Green rust formation
904 controls nutrient availability in a ferruginous water column. *Geology* **40**, 599–602. Available at:
905 http://geology.gsapubs.org/cgi/doi/10.1130/G32959.1.

906 Zirks E., Krom M. D., Zhu D., Schmiedl G. and Goodman-Tchernov B. N. (2019) Evidence for the
907 presence of an oxygen depleted Sapropel Intermediate Water across the Eastern
908 Mediterranean during Sapropel S1. *ACS Earth Sp. Chem.*, A-K. Available at:

https://pubs.acs.org/doi/10.1021/acsearthspacechem.9b00128.

Van Der Zwaan G. J., Duijnstee I. A. P., den Dulk M., Ernst S. R., Jannink N. T. and Kouwenhoven T. J. (1999) Benthic foraminifers: Proxies or problems? A review of paleocological concepts. *Earth Sci. Rev.* **46**, 213–236.

Zwiep K. L., Hennekam R., Donders T. H., van Helmond N. A. G. M., de Lange G. J. and Sangiorgi F. (2018) Marine productivity, water column processes and seafloor anoxia in relation to Nile discharge during sapropels S1 and S3. *Quat. Sci. Rev.* **200**, 178–190. Available at: https://doi.org/10.1016/j.quascirev.2018.08.026.

Figure Legends:

Figure 1: Map of the Eastern Mediterranean Levantine basin with core locations for EZ17G5 and ME0318 (the two cores sampled in this study in green), and PS009PC, SL112, 9509, and MD04-2722 in red.

Figure 2. Age models for cores EZ17G5 and ME0318, showing depth (cm) against age (cal. ka BP).

Figure 3: Total organic carbon (TOC), Ba/Al, Mo/Al, U/Al, V/Al, Mn/Al and Fe_T/Al for ME0318 (left) and EZ17G5 (right). TOC is given in wt%. Ba/Al, Mo/Al, U/Al, V/Al, Mn/Al and Fe_T/Al are shown in 10^{-4} g/g. Dashed lines on RSTM plots represent average shale values (Turekian and Wedepohl, 1961). Light gray shaded box represents the interruption of the sapropel at ~8.2 ka BP. Middle grey shaded boxes represent dysoxic conditions and dark grey boxes anoxic conditions.

Figure 4: Benthic foraminifera number per gram (BFN), Shannon-Wiener diversity and oxygen index (OI) for ME0318 (left) and EZ17G5 (right). Benthic foraminifera were selected from the >125 μm fraction and are displayed as numbers/g. Note the different axes for BFN as indicated by the dashed line for better display of low BFN.

Figure 5: Iron speciation data for ME0318 (left) and EZ17G5 (right). All data are given in μmoles/g.

Figure 6: Fe_{HR}/Fe_T and Fe_{sul}/Fe_{HR} ratios for ME0318 (left) and EZ17G5 (right). All data are given in μmoles/g. The dashed lines at 0.38 (Fe_{HR}/Fe_T) and 0.6 (Fe_{sul}/Fe_{HR}) represent the lower threshold values for identifying water column anoxia and euxinia, respectively (Benkovitz et al., 2020; Poulton and Canfield, 2011).

Figure 7: Phosphorus speciation for ME0318 (left) and EZ17G5 (right). All data are given in μmoles/g.

Figure 8: Plot of Mo_{EF} versus U_{EF} for samples from cores EZ17G5 and ME0318 (after Algeo and Tribovillard, 2009; Tribovillard et al., 2012). Enrichment factors (EF) were calculated relative to average shale (Turekian and Wedepohl, 1961). The modern seawater Mo_{EF}/U_{EF} ratio (Tribovillard et al., 2012) is represented by the solid black line. Dashed lines correspond to multiples of the Mo_{EF}/U_{EF} ratio.

Figure 9: Molar TOC/P_{org} and $TOC/P_{reactive}$ ratios for EZ17G5 (black) and ME0318 (red). Blue line represents the Redfield ratio of 106:1.

Figure 10: Cartoon summarizing the development of the OMZ off the S.E. Levantine basin coastal shelf during the early Holocene (6.8-10.2 kyr BP), showing the position of cores marked in red. The green arrows symbolize the export of organic matter produced in the photic zone into deeper water.

Fig 1

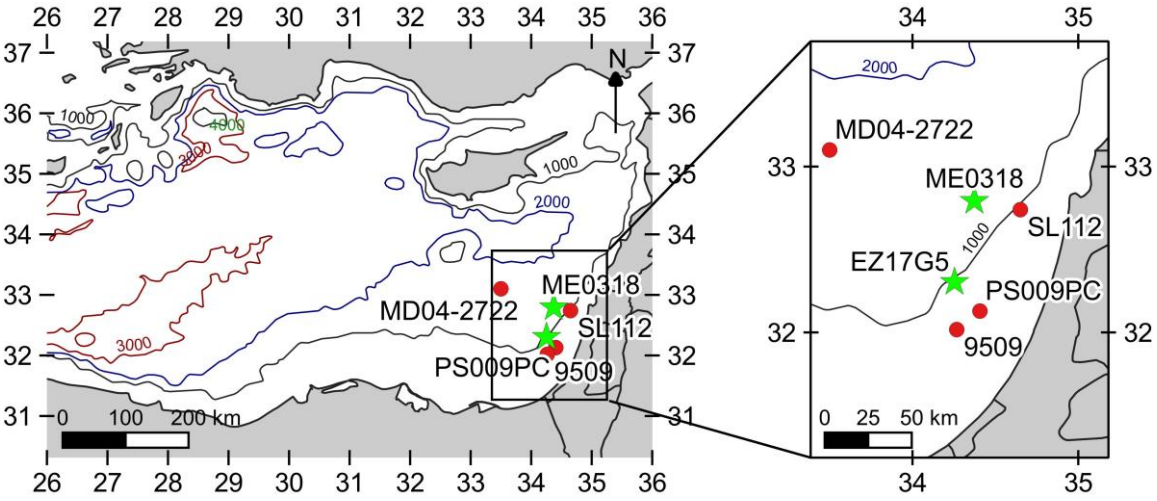
26 27 28 29 30 31 32 33 34 35 36
37 36 35 34 33 32 31
N
1000
4000
2000
3000
MD04-2722
ME0318
SL112
PS009PC
9509
0 100 200 km
34 35
33 32
2000
1000
0 25 50 km

Fig. 2

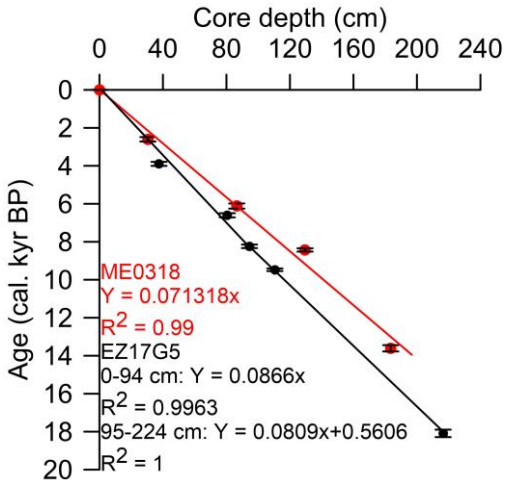
Core depth (cm)
0 40 80 120 160 200 240
Age (cal. kyr BP)
0 2 4 6 8 10 12 14 16 18 20
ME0318
Y = 0.071318x
R2 = 0.99
EZ17G5
0-94 cm: Y = 0.0866x
R2 = 0.9963
95-224 cm: Y = 0.0809x+0.5606
R2 = 1

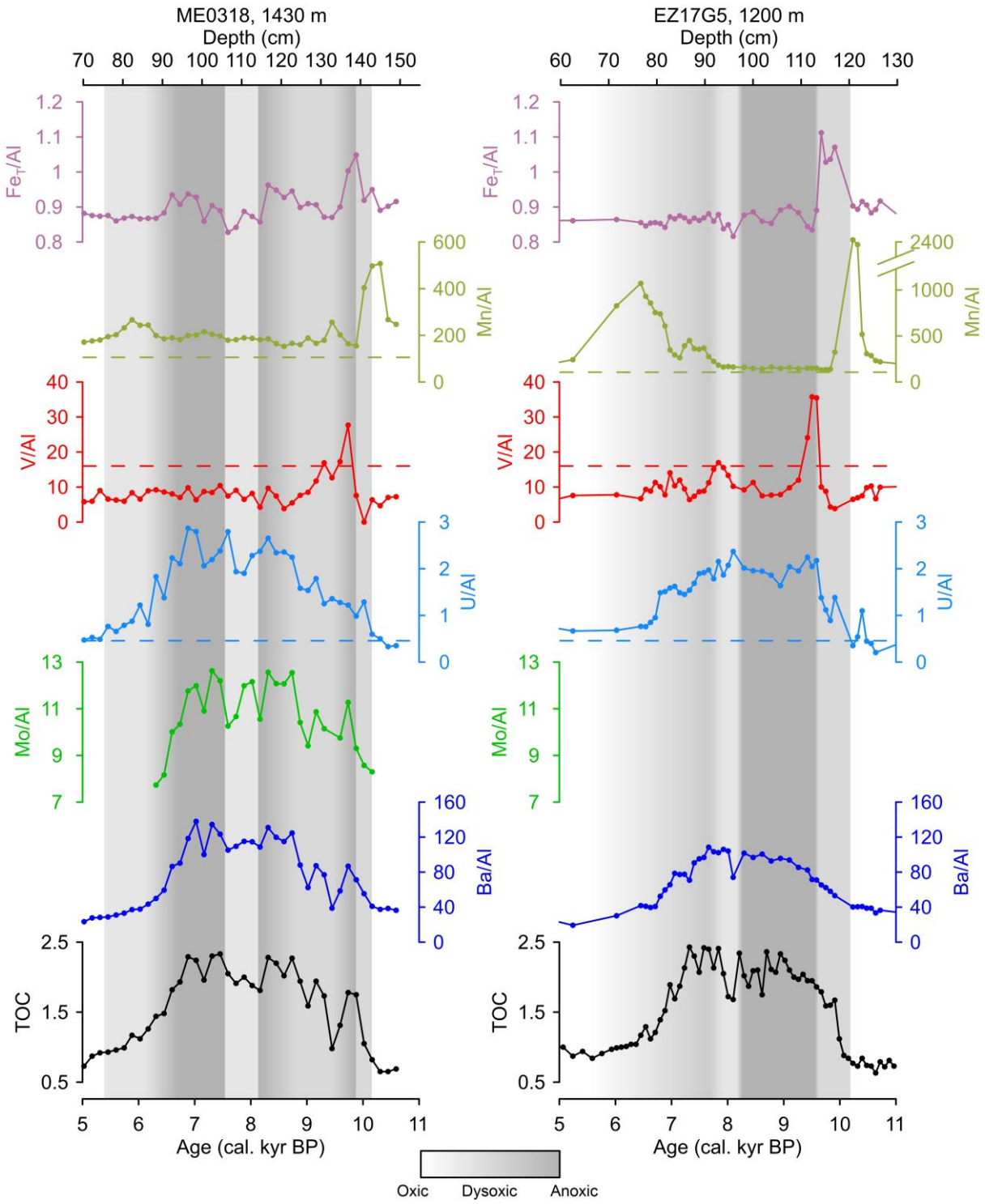
ME0318, 1430 m
Depth (cm)
70 80 90 100 110 120 130 140 150
EZ17G5, 1200 m
Depth (cm)
60 70 80 90 100 110 120 130
Fe$_T$/Al
1.2 1.1 1 0.9 0.8
Mn/Al
600 400 200 0
2400 1000 500 0
V/Al
40 30 20 10 0
U/Al
3 2 1 0
Mo/Al
13 11 9 7
Ba/Al
160 120 80 40 0
TOC
2.5 1.5 0.5
5 6 7 8 9 10 11
Age (cal. kyr BP)
Oxic
Dysoxic
Anoxic

Fig. 4

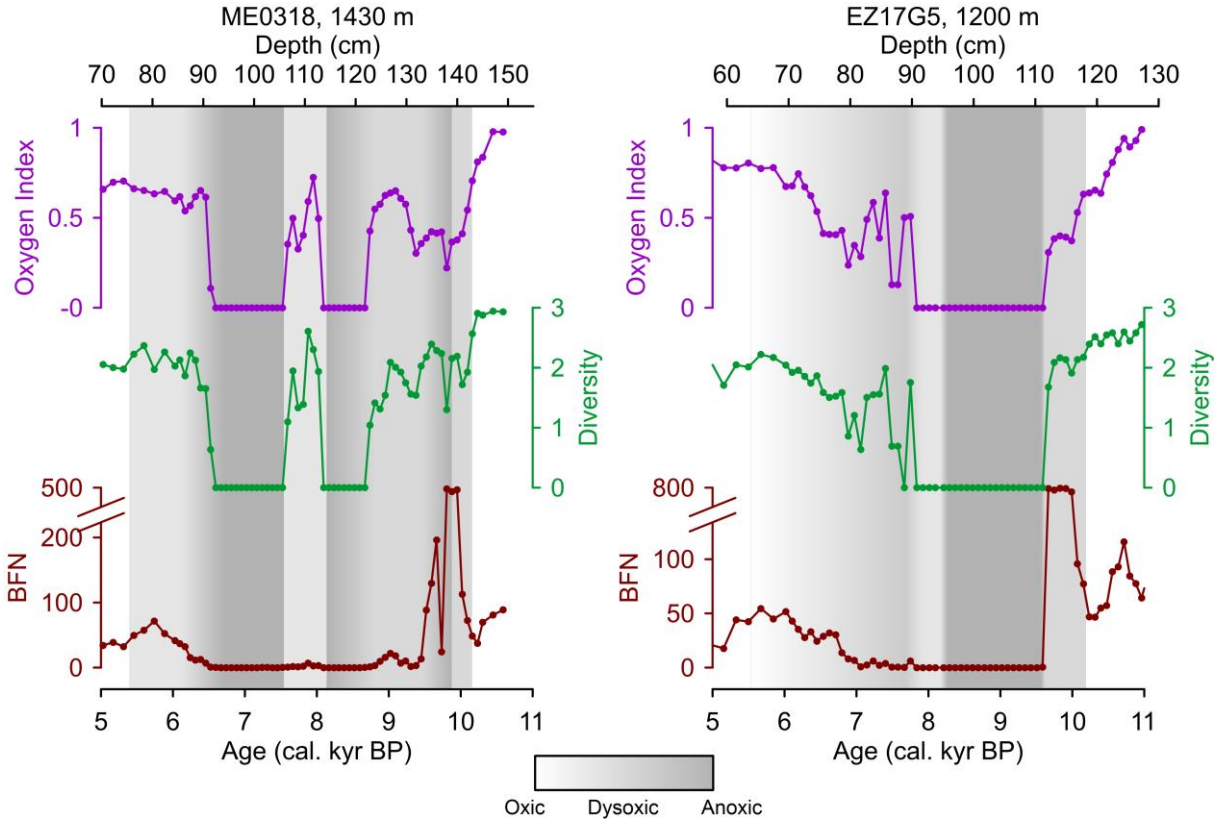
ME0318, 1430 m
Depth (cm)
70 80 90 100 110 120 130 140 150
Oxygen Index
1
0.5
-0
Diversity
3
2
1
0
BFN
500
200
100
0
5 6 7 8 9 10 11
Age (cal. kyr BP)
EZ17G5, 1200 m
Depth (cm)
60 70 80 90 100 110 120 130
Oxygen Index
1
0.5
0
Diversity
3
2
1
0
BFN
800
100
50
0
5 6 7 8 9 10 11
Age (cal. kyr BP)
Oxic
Dysoxic
Anoxic

993 Fig. 5

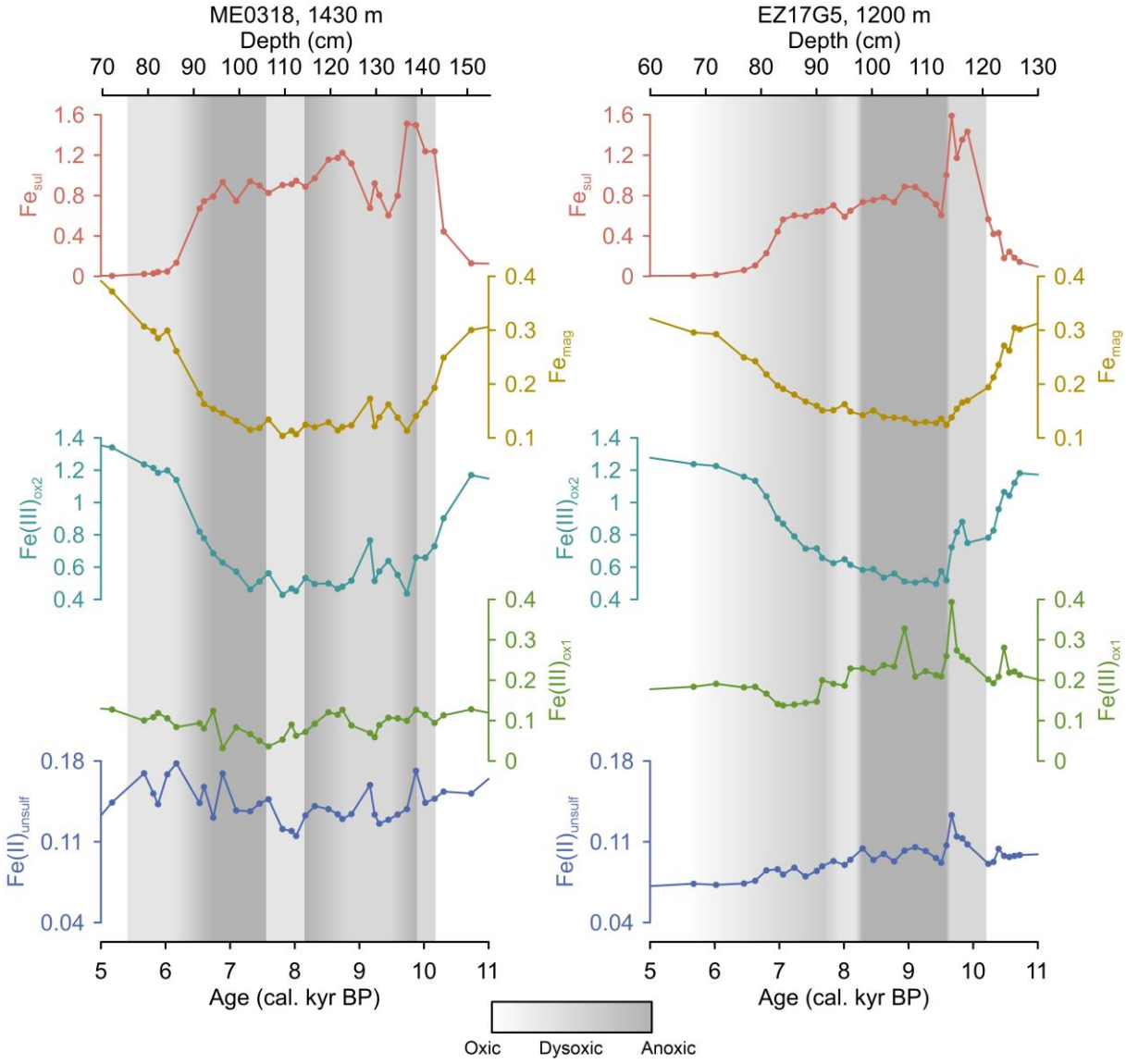

994
995
996
997
998
999
1000
1001
1002
1003
1004
1005

Fig. 6

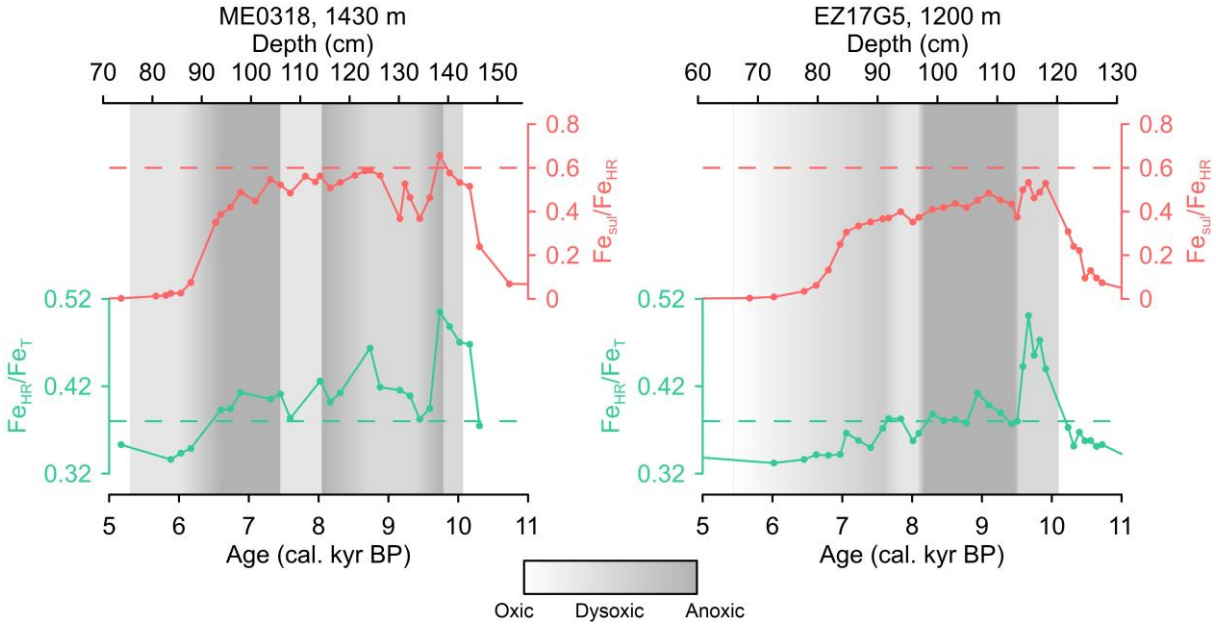
ME0318, 1430 m
Depth (cm)
70 80 90 100 110 120 130 140 150
EZ17G5, 1200 m
Depth (cm)
60 70 80 90 100 110 120 130
0.8
0.6
0.4
0.2
0
Fe_sul/Fe_HR
0.52
0.42
0.32
Fe_HR/Fe_T
5 6 7 8 9 10 11
Age (cal. kyr BP)
Oxic
Dysoxic
Anoxic

Fig. 7

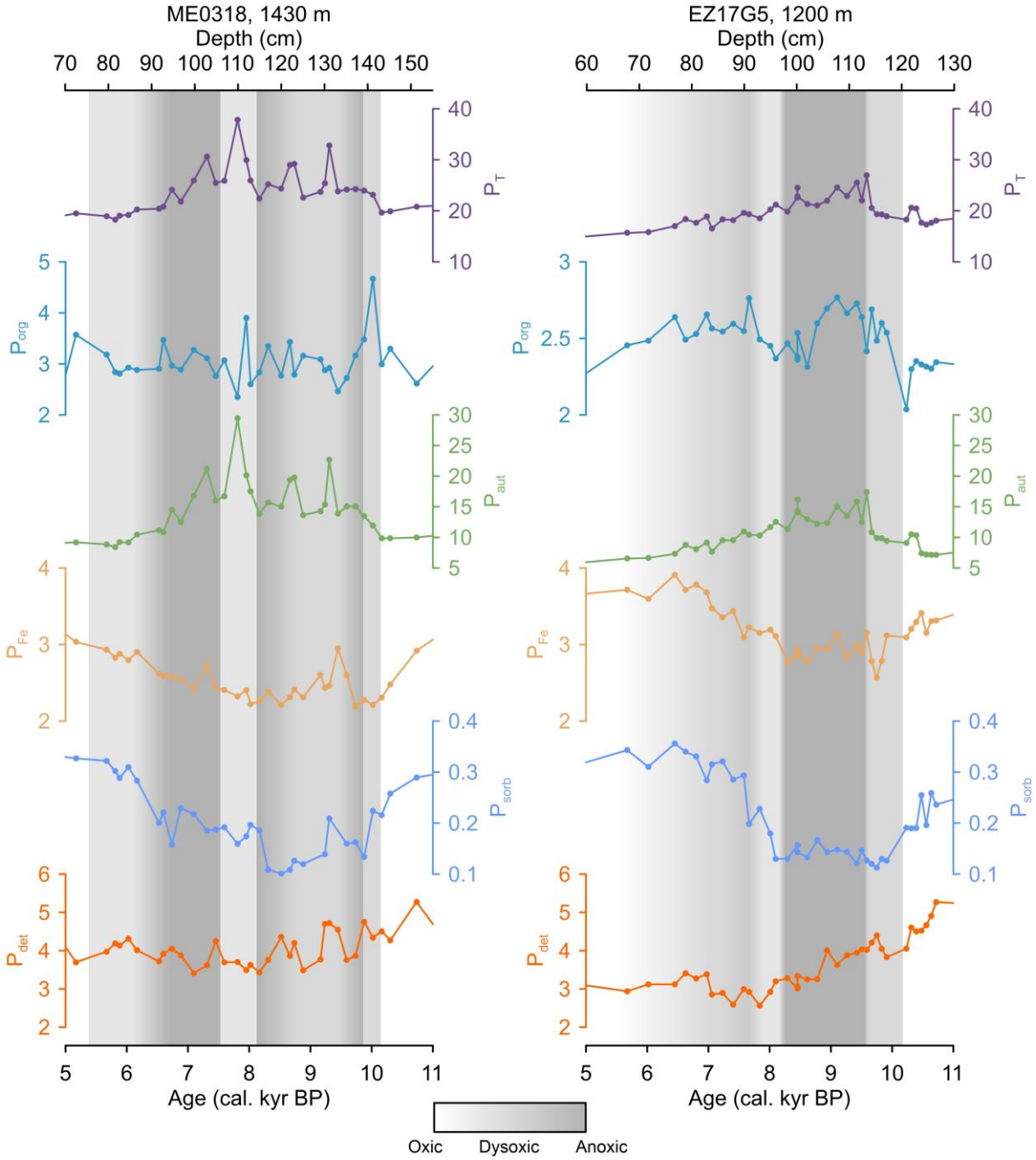
ME0318, 1430 m
Depth (cm)
70 80 90 100 110 120 130 140 150
EZ17G5, 1200 m
Depth (cm)
60 70 80 90 100 110 120 130
P_T
P_org
P_aut
P_Fe
P_sorb
P_det
5 6 7 8 9 10 11
Age (cal. kyr BP)
Oxic
Dysoxic
Anoxic

1038 Fig. 8

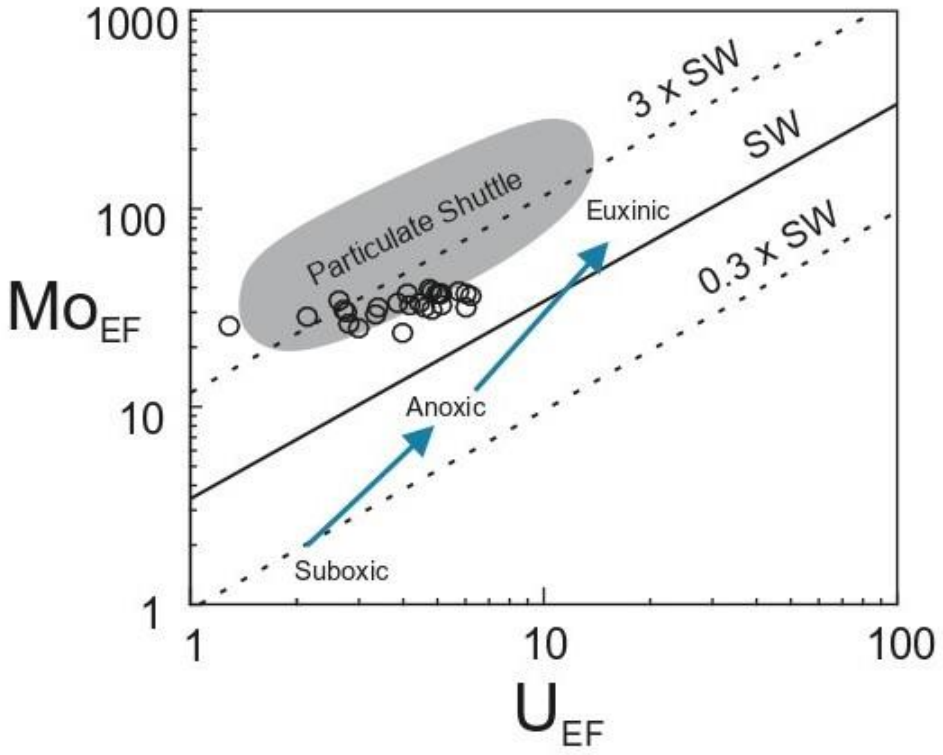

1039

1040 Fig. 9

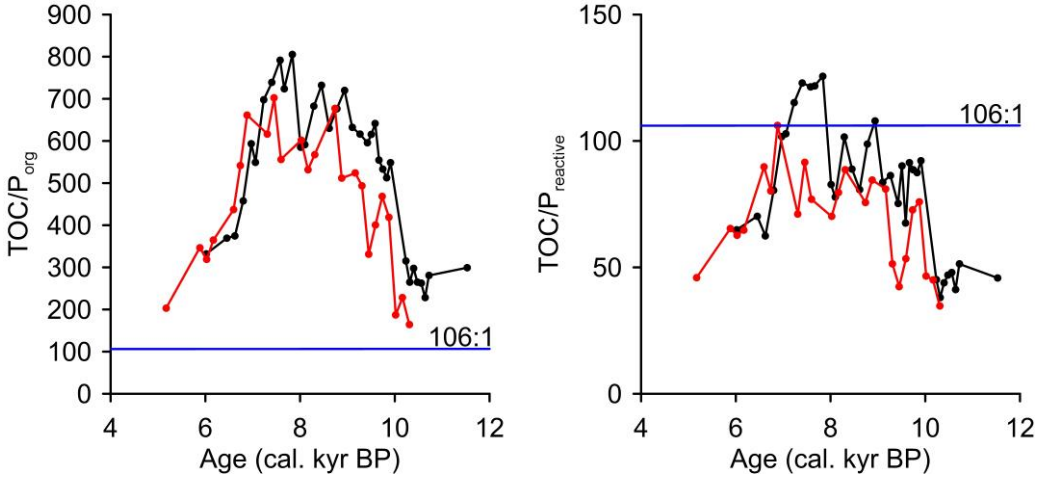

1041

1042

1043

1044

1045

1046 Fig. 10

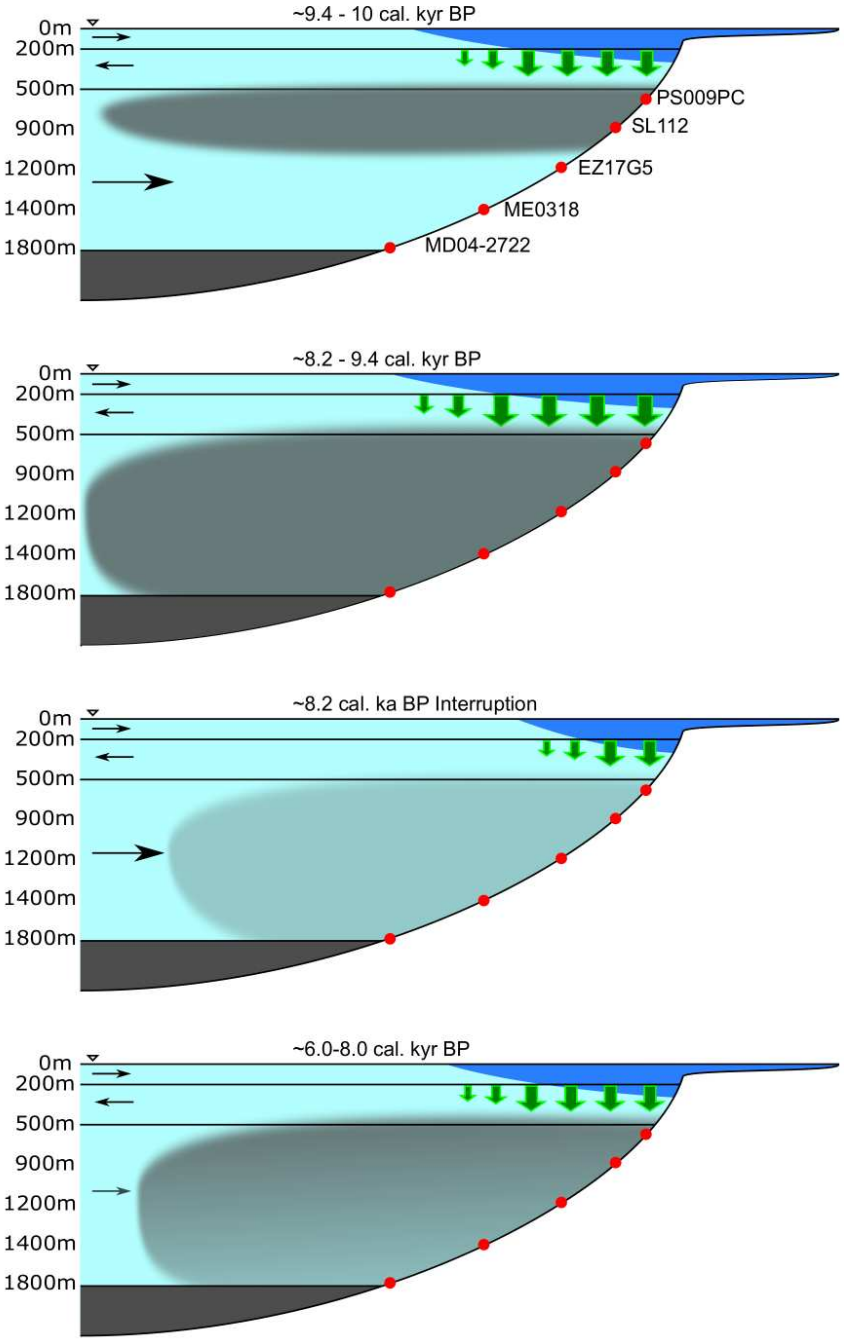

1047

1048

1049